Received: 24 July 2021 | Revised: 11 October 2021 | Accepted: 9 November 2021

DOI: 10.1002/ett.4415

RESEARCH ARTICLE

WILEY

Performance limits of wireless powered cooperative NOMA over generalized fading

Galymzhan Nauryzbayev[1] | **Orken Omarov**[1] | **Sultangali Arzykulov**[2] | **Khaled M. Rabie**[3] | **Xingwang Li**[4] | **Ahmed M. Eltawil**[2]

[1]Department of Electrical and Computer Engineering, School of Engineering and Digital Sciences, Nazarbayev University, Nur-Sultan, Kazakhstan

[2]Computer, Electrical and Mathematical Science and Engineering Division, King Abdullah University of Science and Technology, Thuwal, Saudi Arabia

[3]Department of Engineering, Manchester Metropolitan University, Manchester, UK

[4]School of Physics and Electronic Information Engineering, Henan Polytechnic University, Jiaozuo, China

Correspondence
Galymzhan Nauryzbayev, Department of Electrical and Computer Engineering, School of Engineering and Digital Sciences, Nazarbayev University, 53, Kabanbay Batyr Avenue, Nur-Sultan 010000, Kazakhstan.
Email: galymzhan.nauryzbayev@nu.edu.kz

Funding information
Nazarbayev University, Faculty Development Competitive Research Program, Grant/Award Number: 240919FD3935

Abstract

The non-orthogonal multiple access (NOMA) technique is a prospective solution to support the massive connectivity of an ever-increasing number of wirelessly connected devices and address the spectrum scarcity issue. In this article, the outage probability and ergodic capacity of a two-hop cooperative NOMA network with an energy-limited relaying node are quantified over a generalized $\alpha - \kappa - \mu$ statistical model. The relay acts in an amplify-and-forward mode and performs energy harvesting (EH) using the time-switching and power splitting relaying protocols. Moreover, the impact of hardware impairments (HIs) is incorporated into the performance evaluation. The obtained results prove the importance of HIs and allow one to evaluate the outage probability and ergodic capacity over various statistical models and system parameters. Finally, the results suggest that the optimal performance at a specific scenario depends on the combination of multiple factors, such as channel conditions, HI level, transmit power, and EH protocol.

1 | INTRODUCTION

The low latency, high data rate and reliability are the integral parts of emerging communication standards.[1] These system requirements can be resolved by exploiting the millimeter-wave (mmWave) technology considered as the essential of fifth-generation (5G) communication networks.[2] Despite its advantages, the mmWave communication has some limitations; for instance, the main issue lies in the bounded coverage area due to the exploited high-frequency bands,[3] which, in turn, requires line-of-sight (LoS) communication links. However, these days it is rare to have LoS channels in urban areas, where 5G is about to be deployed. The negative impact of such a limitation can be potentially mitigated using cooperative communication principles.[4] In addition to that, it is forecast that the traffic exchanged wirelessly will reach its all-time maximum very soon,[5] whereas the spectrum scarcity has not been finally solved yet.

1.1 | Related works

1.1.1 | Non-orthogonal multiple access (NOMA)

Powered by successive interference cancellation (SIC), the NOMA technique is widely identified as a main technology able to mitigate the spectrum shortage via co-sharing the common resources.[6] There two main group of NOMA such as power domain (PD) and code domain (CD). In PD-NOMA, different users are allocated with different power levels according to their channel conditions.[7] For instance, a "weaker" user performs SIC by decoding the message of a more "robust" user and extracting it first before processing its own message. Ding et al[8] showed that PD-NOMA has a beneficial effect on improving the network performance metrics. For example, Liang et al[9] quantified the performance of cooperative NOMA, while the other researchers[10] showed the enhanced spectral efficiency (SE) of PD-NOMA. Additionally, a similar network architecture was considered, where the authors demonstrated a performance increase through the implementation of relay-assisted PD-NOMA networks.[11] These results suggested the benefits of using relaying methods in PD-NOMA networks for Internet-of-Things (IoT) applications. In CD-NOMA, different users are assigned different codes, and are then multiplexed over the same time-frequency resources. The most popular type of CD-NOMA is the sparse code multiple access (SCMA), where multiple users are allocated with different sparse codewords and a message passing algorithm can be used to realize multi-user detection.[12,13] For example, Farhadi Zavleh et al[14] investigated codebook assignment and power allocation for a SCMA-based cloud radio access network. Further, the same authors[15] studied a three-step resource allocation algorithm to achieve the maximum total sum rate subject in SCMA-based network. The main difference between PD-NOMA and CD-NOMA is the fact that the latter can achieve better system performance at the cost of increased signal bandwidth and receiver complexity. The SCMA-based receiver usually has higher complexity than a SIC-based PD-NOMA receiver.[16] Hence, we consider the downlink PD-NOMA method in our article and refer as the NOMA henceforward throughout the article.

1.1.2 | Cooperative networks and energy harvesting

The cooperative network was first defined as a network architecture,[17] where the node's resources are deliberately spent to deliver the information to end-users via multiple mutually independent channels by forming a spatial diversity. Ding et al[18] and Liu et al[19] considered several NOMA applications in cooperative networks. For instance, in the former work,[18] the authors showed the improvement of outage probability (OP) in cooperative NOMA with respect to its non-cooperative counterpart. Similarly, in the latter,[19] the authors demonstrated that the performance of cooperative NOMA is superior in comparison to non-cooperative NOMA under different user selection methods. The network cooperativeness is widely applicable to the scenarios, when transmission sessions are susceptible to a fading phenomenon and the nodes are deployed with single antennas without capabilities of beamforming. Furthermore, the applications, for example, IoT, biomedical sensors and surveillance, are subject to energy constraints due to being battery-powered, which can be addressed by incorporating wireless power transfer techniques.

Having said this, it is pertinent to note that one of the candidates to resolve the energy scarcity is simultaneous wireless information and energy transfer (SWIPT). Its core idea was introduced in the work of Varshney,[20] and the most popular two methods for energy harvesting (EH) are the power-splitting relaying (PSR)[21,22] and time-switching relaying (TSR)[23] protocols. These protocols are maintained via partitioning the available resources in power and time domains. For example, Xu et al[21] showed that the SE of cooperative SWIPT-enabled NOMA networks is superior compared to the other transmission architectures, such as non-cooperative NOMA and OMA at low transmit power scenarios. Furthermore, they revealed that, unlike SWIPT-enabled cooperative NOMA, the achievable data rate of a relaying user degrades significantly in non-cooperative NOMA, as the target rate of an end-user increases. Moreover, Yang et al[24] revealed that cooperative NOMA with SWIPT outperforms its OMA counterpart in terms of the outage probability under certain power allocation (PA) factors.

1.1.3 | Generalized fading models

The wireless medium available for communication purposes by mobile nodes undergoing dense deployment is often characterized by Rayleigh fading channels due to the present scattering and reflections.[25] At the same time, to devise plant

application scenarios, Johansson et al[26] considered the Rayleigh fading to quantify the performance of a system model with an ultra-reliable and low-latency communication. On the other hand, the effects of LoS and non-line-of-sight (NLoS) signals can be taken into account using Rician fading for visible light communications (VLC) networks.[27,28] Pan et al[29] considered the system model incorporating the RF and VLC communication and applied the Rician model due to the uncertainty in nodes' positions. Furthermore, the Nakagami-m and Weibull were suggested as propagation models for the theoretical evaluation of communication performance on the 800-900 MHz range.[30] The vehicle-to-vehicle communication was described by a means of Weibull fading,[31] where the small-scale fading was described by encountering an urban environment. Similarly, small-scale Nakagami-m fading is often exploited to consider multipath clusters in many applications, for example, mmWave communication.[32]

1.1.4 | Residual hardware impairments (HIs)

Schenk[33] proved the importance of considering the imperfections related to hardware of radio-frequency (RF) transceivers, especially, when operating with high-frequency signals. Although some algorithms are developed to combat the effect of HIs, certain types of HIs cannot be fully suppressed.[34] In Reference 35, the authors analyzed the two-hop network performance under different relaying architectures, where residual HIs at all nodes were considered. It highlighted the HIs level parameters applicable to a real-world scenarios and estimated the performance metrics such as ergodic capacity and outage probability. In References 36,37, a two-hop relaying network was studied, where the authors considered the HI effect, called quadrature and in-phase imbalance, at the RF front-ends of amplify-and-forward (AF) relays. They quantified the performance through outage probability and used the complex Gaussian statistic to describe the combined effect of HIs. A similar way of describing HIs and network design was implemented.[38] Having all the mentioned above, it is clear that considering the hardware impairments during the network performance evaluation is essential.

1.2 | Motivation and main contributions

The information sent over wireless medium are exposed to various channel realizations described by various statistical models. In References 39-41, the authors provided the performance results for dual-hop cooperative NOMA over Rayleigh and Weibull channels, respectively. Moreover, outage probability and ergodic capacity performance of the SWIPT-enabled cooperative NOMA system were studied in Reference 42, where the channel was modeled as Nakagami-$m$fading. Further, Kumar et al[43] and Arzykulov et al[44] analyzed the performance of two-hop cooperative NOMA networks, where they expressed the wireless channels through a generalized $\alpha - \mu$ fading model. In contrast to References 41,43, this article uses the generalized α-κ-μ fading model to estimate the performance of two-hop cooperative NOMA, which includes $\alpha - \mu$, $\kappa - \mu$, Rice, Rayleigh, Weibull and Nakagami-m fading models as its special cases. Additionally, the authors in the latter work[43] assumed a constant power source at the cooperative agent and omitted the hardware imperfections. Similarly, another work[45] applied generalized $\alpha - \eta - \mu$ fading to simulate the channel properties but focused on the perfect network conditions. Moreover, there is no compound consideration of the transmit SNR, the channel conditions, imperfect SIC and HI's level of transceivers to identify the optimal energy harvesting protocol for a cooperative relaying agent. Therefore, to obtain a more practical performance evaluation of the two-hop cooperative NOMA networks, the impact of imperfect SIC and transceiver HI level will be studied in this article.

The key contributions of this work are as follows:

- The expressions of the outage probability and ergodic capacity are derived for dual-hop cooperative NOMA over a generalized α-κ-μ fading model, while considering the HI level of transceivers. The derived analytical expressions demonstrate the advantage of cooperative NOMA over its orthogonal multiple access (OMA) counterpart. Moreover, the correctness of findings are verified via thorough Monte-Carlo simulations.
- The derived expressions for the outage probability and ergodic capacity account for the non-homogeneity of fading channels represented through specific cases of α-κ-μ generalized model, which signify that the transmitted message is exposed to diverse channel properties described by various statistical models during the whole transmission time block.

TABLE 1 Nomenclature

Parameter	Value	Parameter	Value	Parameter	Value
Source	S	HI level	Υ_j	Distance between nodes	d
NOMA user i	U_i	HI level variance	$\mathfrak{z}_j^2$	SNR-associated rate threshold	v_i
NOMA message	x_i	Multipath clusters	μ	Power ratio of the LoS and scattered signals	κ
PA factor	α_i	AWGN	n_i	Modified Bessel function of the νth order	$I_\nu(\cdot)$
Channel coefficient	h	AWGN variance	σ_i^2	End-to-end data transmission time	T
Transmit power at S	P_S	Expectation operator	$\mathbb{E}[\cdot]$	TSR or PSR indicator	p
Path-loss coefficient	τ	Amplification factor	G_p	Energy harvesting efficiency	ϖ
Ergodic capacity	C_{erg}	Rate threshold	$\mathcal{I}_{\text{th},i}$	Time portion for harvesting	η
SINDR at U_i	γ_{U_i}	PDF of RV X	$f_X(\cdot)$	Power portion for harvesting	ρ
Probability	$\Pr[\cdot]$	CDF of RV X	$F_X(\cdot)$	Imperfect SIC parameter	ς

- To obtain valuable insights from the analytical findings, their asymptotic behavior is studied for the OP expressions over a generalized α-κ-μ fading model.
- The analytical expressions obtained for the outage probability and ergodic capacity can describe the effect of multiple system parameters, such as distances, EH factors, imperfect SIC and HI level on the network performance of cooperative NOMA. This allows one to deduce the communication performance explicitly to certain system characteristics and environmental factors described by α, κ, and μ parameters.

1.3 | Notations and article organization

Notation: The following notations are applied to the rest of the article. The Gamma and lower incomplete Gamma functions are defined as $\Gamma(a) = \int_0^\infty t^{a-1}e^{-t}\mathrm{d}t$, as in eq. (8.310.1),[46] and $\gamma(a,x) = \int_0^x t^{a-1}e^{-t}\mathrm{d}t$, as in eq. (8.350.1),[46] accordingly. The Meijer's G-function is denoted by $G_{p,q}^{m,n}\left(z\middle|\begin{matrix}(a_p)\\(b_q)\end{matrix}\right)$, as in eq. (5),[47] and $\Delta(k,a) = \frac{a}{k}, \frac{a+1}{k}, \ldots, \frac{a+k-1}{k}$, as in eq. (22).[47] Also, all parameters defined in this article are presented in Table 1.

Organization: The article's remainder is structured as follows. Section 2 introduces the cooperative NOMA network, while Sections 3 and 4 present the analysis of ergodic capacity and outage probability over the generalized fading model, accordingly. Section 5 presents the results for a variety of channel and HI parameters and supports them with simulations. Finally, Section 6 concludes and briefly summarizes the work findings.

2 | SYSTEM AND CHANNEL MODELING

2.1 | System topology

Consider a cooperative NOMA network depicted in Figure 1, comprising the source (S) and two receiver nodes, denoted by U_1 and U_2, where U_1 plays a role of a cooperative agent working in the AF mode. The nodes are assumed to be deployed with single antennas and operate in the downlink half-duplex regime. Exploiting the NOMA principle, S transmits a compound message $x_s = \sum_i \sqrt{a_i P_S} x_i$, where P_S is the transmit power at S; a_i and x_i denote the PA factor and corresponding message designated to a certain receiver i, respectively. For the considered network scenario, we assume that the channel are given by $h_1 > h_2$ due to a relatively close proximity of S to U_1. Therefore, the PA coefficients are set to be as $a_1 < a_2$ following the power-domain NOMA approach. The S-to-U_1, U_1-to-U_2 and S-to-U_2 channel links* are given by the independent RVs h_1, h_2, and h_3, respectively; the respective distances are denoted by d_1, d_2, and d_3, accordingly. To enhance its performance, U_2 deploys a maximum ratio combining (MRC) technique, which operation requires perfect CSI allowance.

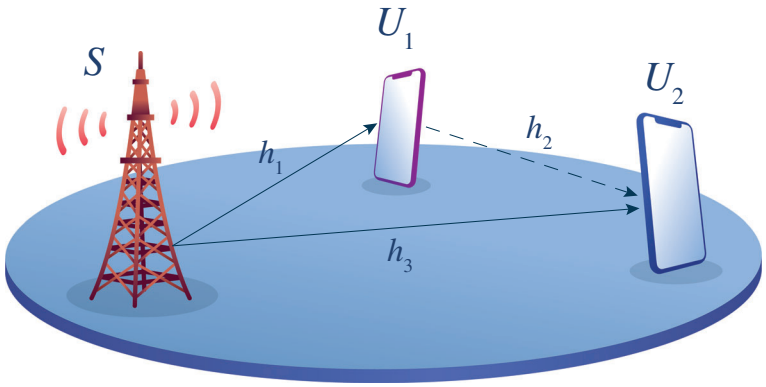

FIGURE 1 An illustration of the considered two-hop cooperative NOMA, where solid and dashed lines indicate the direct and cooperative links, respectively

In this work, the channel state fluctuations are defined using the generalized α-κ-$\mu^{\dagger}$ fading model, with PDF

$$f_{h_i}(r) = \frac{\alpha_i \kappa_i^{\frac{1-\mu_i}{2}} \mu_i (1+\kappa_i)^{\frac{1+\mu_i}{2}}}{e^{\mu_i(\kappa_i + r^{\alpha_i} + \kappa_i r^{\alpha_i})}} r^{\frac{\alpha_i(1+\mu_i)}{2}-1} I_{\mu_i - 1}\left(2\mu_i \sqrt{\kappa_i(1+\kappa_i)} r^{\frac{\alpha_i}{2}}\right), \tag{1}$$

where κ is the power ratio of the LoS and scattered signals while μ and α are the multipath clusters and non-linearity parameter, accordingly. $I_v(\cdot)$ indicates the modified Bessel function[50] of the vth order and first kind.

This article studies the impact of residual HIs observable at the transceivers' front-ends. Each link is characterized by the compound HI level, denoted by Υ_j, with $j = \{s, u_1; u_1, u_2; s, u_2\}$, which is modeled via the complex Gaussian statistics, with variance $\mathfrak{d}_j^2 \triangleq \mathfrak{d}_{j,t}^2 + \mathfrak{d}_{j,r}^2$ (t and r stand for the transmitter's and receiver's HIs levels) and zero-mean.[33]

2.2 | Transmission protocols

Due to the radio broadcast transmission, both users of interest observe the superpositioned NOMA signal as

$$y_i = \sqrt{\frac{P_S}{d_{s,u_i}^{\tau}}} h_{s,u_i} \left(\sum_{\forall j} \sqrt{a_j} x_j + \Upsilon_{s,u_i} \right) + n_i, \ \forall i \in \{1, 2\}, \tag{2}$$

where n_i denotes the additive white Gaussian noise (AWGN) term at U_i, with variance σ_i^2 and zero-mean. τ indicates the path-loss coefficient. Moreover, U_2 obtains another message's replica from the direct link and decodes its own message x_2 using the signal-to-interference-plus-distortion-plus-noise ratio (SINDR) given by

$$\gamma_{U_2}^{\{x_2\}} = \frac{e_1 Z}{e_2 Z + e_3}, \tag{3}$$

where $Z = |h_3|^2$, $e_1 = a_2$, $e_2 = a_1 + \mathfrak{d}_{s,u_2}^2$, and $e_3 = \frac{\sigma_2^2 d_3^{\tau}}{P_s}$.

The overall time required for an end-to-end data transmission is denoted by T. To be more specific, in the PSR, this time is split into two equal parts. The respective first time slot is devoted to the S-to-U_1 transmission, where U_1 harvests the power portion, given by ρP_S, to be used further in the next time slot. The remaining power, that is, $(1-\rho)P_S$, is needed for message decoding purposes. The second time slot is used by U_1 to amplify and then forward the required message to U_2 using the harvested energy. For the TSR case, considering the same T, the time portion ηT ($0 \le \eta \le 1$) is designated for energy harvesting. Moreover, the remaining time is evenly divided to organize the S-to-U_1 and U_1-to-U_2 transmission sessions.

For energy harvesting purposes, the PSR protocol exploits the portion of the received signal given by

$$\sqrt{\rho}y_1 = \sqrt{\frac{\rho P_S}{d_1^\tau}}h_1\left(\sum_{\forall j}\sqrt{a_j}x_j + \Upsilon_{s,u_1}\right) + \sqrt{\rho}n_1. \tag{4}$$

Thus, the harvested energy[‡] is then decided as

$$E_p^H = R_p\left(P_S|h_1|^2\left(1+\ni_{s,u_1}^2\right)d_1^{-\tau} + \sigma_1^2\right), \tag{5}$$

where p is an indicator denoting either TSR or PSR. $0 \le \varpi \le 1$ denotes the energy harvesting efficiency. Furthermore, by disregarding the noise-induced energy, (5) can be made simpler, and the power available for consecutive time slots is defined as $P_p^R = \frac{E_p^H}{H_p T}$ and shown in Table 2. Additionally, the information decoding is processed using the remaining portion of an incoming signal, given by $y_1^{IT} = \sqrt{1-\rho}y_1 + n_c$, where n_c is the AWGN term.

Recalling NOMA, U_1 can perform SIC as follows: it first decodes stronger message x_2, subtracts it and then processes own data x_1 via the utilization of a signal-to-distortion-plus-noise ratio (SDNR) expressed as

$$\gamma_{U_1}^{\{x_1\}} = \frac{b_1 X}{b_2 X + b_3}, \tag{6}$$

where $X = |h_1|^2$, and the other important variables related to both protocols are drawn in Table 2. Note that U_1 only performs SIC, and the impact of imperfect SIC is therefore defined by ς,[52] that is, $\varsigma = 0$, $0 < \varsigma < 1$, and $\varsigma = 1$ indicate the perfect SIC, imperfect SIC, and no SIC cases, respectively.

During the last time slot, U_2 receives the signal forwarded by U_1 as

$$y_{1\to 2} = \frac{G_p h_2}{\sqrt{d_2^\tau}}\left(D_p\left(y_1 - n_1\right) + n_p + \Upsilon_{u_1,u_2}\right) + n_2, \tag{7}$$

where $D_p = \{1; \sqrt{1-\rho}\}$ for the TSR and PSR, respectively. G_p denotes the amplification factor. Assuming the high signal-to-noise ratio (SNR) regime, this factor can be simplified as $G_p = \sqrt{\frac{P_p^R}{W_p}}$, where $W_{p\equiv PSR} = (1-\rho)\left(P_s\left(1+\ni_{s,u_1}^2\right)d_1^{-\tau}|h_1|^2 + \sigma_1^2\right) + \sigma_c^2$, $W_{p\equiv TSR} = \frac{\left(1+\ni_{s,u_1}^2\right)P_S}{d_1^\tau}|h_1|^2 + \sigma_1^2$ and P_p^R along with n_p are shown in Table 2.

Furthermore, substituting these definitions into (7), message x_2 can be decoded using the SINDR given by

$$\gamma_{U_{1\to 2}}^{\{x_2\}} = \frac{c_1 XY}{c_2 XY + c_3 Y + c_4}, \tag{8}$$

where $Y = |h_2|^2$, and the variables c_1, c_2, c_3, and c_4 are shown in Table 2.

TABLE 2 The variables in (6) to (8) for both PSR and TSR protocols

	H_p	n_p	R_p	P_p^R	G_p	b_1
PSR	$1/2$	$\sqrt{1-\rho}n_1 + n_c$	$0.5\varpi\rho T$	$\varpi\rho P_S d_1^{-\tau}\left(1+\ni_{s,u_1}^2\right)\|h_1\|^2$	$\sqrt{\frac{\varpi\rho}{1-\rho}}$	a_1
TSR	$(1-\eta)/2$	$\varpi\eta T$	n_1	$\frac{2\varpi\eta P_S\left(1+\ni_{s,u_1}^2\right)}{(1-\eta)d_1^\tau}\|h_1\|^2$	$\sqrt{\frac{2\varpi\eta}{1-\eta}}$	a_1
	b_2	b_3	c_1	c_2	c_3	c_4
PSR	$\ni_{s,u_1}^2 + \varsigma a_2$	$\frac{d_1^\tau}{P_S}\left(\sigma_1^2 + \frac{\sigma_c^2}{1-\rho}\right)$	a_2	$a_1 + \ni_{s,u_1}^2$	$\frac{d_1^\tau}{P_S}\left(\sigma_1^2 + \frac{\sigma_c^2+\ni_{u_1,u_2}^2}{(1-\rho)}\right)$	$\frac{d_1^\tau d_2^\tau \sigma_2^2}{\varpi\rho P_S}$
TSR	$\ni_{s,u_1}^2 + \varsigma a_2$	$\frac{d_1^\tau\sigma_1^2}{P_S}$	a_2	$a_1 + \ni_{s,u_1}^2$	$\frac{d_1^\tau}{P_S}\left(\sigma_1^2 + \ni_{u_1,u_2}^2\right)$	$\frac{\sigma_2^2}{P_S}\frac{d_1^\tau d_2^\tau(1-\eta)}{2\varpi\eta}$

3 | OUTAGE PERFORMANCE

The outage event is declared at U_i if its achievable data rate falls lower than a pre-defined rate threshold, denoted by $\mathcal{I}_{\text{th},i}$, and can be written as

$$P_{\text{out},i} = \Pr\left[\gamma_{U_i}^{[\text{eff}]} < v_i\right], \tag{9}$$

where $v_i = 2^{\frac{\mathcal{I}_{\text{th},i}}{H_p}} - 1$ stands for a predefined SNR-associated rate threshold, and $\gamma_{U_i}^{[\text{eff}]}$ denotes the resultant SINDR at U_i.

The outage performance of U_1 is defined as

$$P_{\text{out},1} = \Pr\left[\gamma_{U_1}^{[\text{eff}]} < v_1\right] = \Pr\left[X < \frac{v_1 b_3}{b_1 - v_1 b_2}\right] = \sum_{m=0}^{m_\infty} \frac{(\mu_1\kappa_1)^m \gamma\left(\mu_1 + m, \Phi_1\left(\frac{v_1 b_3}{b_1 - v_1 b_2}\right)^{\frac{\alpha_1}{2}}\right)}{m!\Gamma(\mu_1 + m)e^{\mu_1\kappa_1}}, \tag{10}$$

where $\Phi_i = \mu_i(1 + \kappa_i)$, and $f_X(x)$ is found in Appendix A.

The outage performance of U_2 can be refined by a means of MRC by incorporating both signals arriving via direct and relay links as

$$P_{\text{out},2} = \Pr\left[\gamma_{U_2}^{[\text{eff}]} < v_2\right] = \Pr\left[W_1 + W_2 < v_2\right] = \int_0^\infty \int_0^{v_2 - w_1} f_{W_1,W_2}(w_1, w_2)\mathrm{d}w_2\mathrm{d}w_1 = \int_0^\infty F_{W_2}(v_2 - v) f_{W_1}(v)\mathrm{d}v, \tag{11}$$

where $W_1 = \frac{e_1 Z}{e_2 Z + e_3}$ and $W_2 = \frac{c_1 XY}{c_2 XY + c_3 Y + c_4}$. Moreover, F_{W_2} is the cumulative distribution function (CDF) of W_2 and $f_{W_1,W_2}(w_1, w_2)$ is the joint PDF of W_1 and W_2. After several algebraic manipulations shown in Appendix B, we obtain the expression shown in (12), where $A = \frac{\alpha_2 \mu_2^{2n+\mu_2} \kappa_2^n (1+\kappa_2)^{n+\mu_2}}{2n!\Gamma(n+\mu_2)e^{\mu_2\kappa_2}}$, $K_2 = \Phi_2\left(\frac{\Phi_1\alpha_1}{\alpha_2}\right)^{\frac{\alpha_2}{2}}\left(c_4 c_3^{\frac{\alpha_1}{2}-1}\right)^{\frac{\alpha_2}{2}}$, and $F_2 = \frac{c_4^{\frac{\alpha_2(\mu_2+n)}{2}}\sqrt{\frac{2}{\alpha_2}}}{(2\pi)^{\frac{\alpha_2}{4}-0.5}} c_3^{\frac{\alpha_1 p}{2} + \frac{(\alpha_1-2)(\alpha_2(\mu_2+n)-2s)}{4}} \left(\frac{\Phi_1\alpha_1}{\alpha_2}\right)^{\frac{\alpha_2(\mu_2+n)}{2}-s}$.

$$\begin{aligned} P_{\text{out},2} = 1 - \sum_{n=0}^{n_\infty}\sum_{m=0}^{m_\infty} \frac{A(\mu_1\kappa_1)^m}{m!e^{\mu_1\kappa_1}} \sum_{p=0}^{\mu_1+m-1} \frac{(\Phi_1)^p}{p!} \sum_{s=0}^{\frac{\alpha_1 p}{2}} \frac{\frac{\alpha_1 p}{2}! F_2}{(\frac{\alpha_1 p}{2} - s)!s!} \Phi_3^{\mu_3} \frac{e_1\alpha_3\mu_3\sqrt{\kappa_3(1+\kappa_3)}}{2\left(\mu_3\sqrt{\kappa_3(1+\kappa_3)}\right)^{\mu_3}} \\ \times \int_0^\infty \left(\frac{v_2 - v}{c_1 - (v_2 - v)c_2}\right)^{\frac{2\alpha_1(p-s)+\alpha_1\alpha_2(\mu_2+n)+4s}{4}} \left(\frac{e_3 v}{e_1 - e_2 v}\right)^{\frac{\alpha_3(\mu_3+1)}{4}} e^{-\left(\Phi_1\left(\frac{(v_2-v)c_3}{c_1-(v_2-v)c_2}\right)^{\frac{\alpha_1}{2}} + \kappa_3\mu_3 + \Phi_3\left(\frac{e_3 v}{e_1 - e_2 v}\right)^{\frac{\alpha_3}{2}}\right)} \\ \times \frac{I_{\mu_3-1}\left(2\mu_3\sqrt{\kappa_3(1+\kappa_3)}\left(\frac{e_3 v}{e_1 - e_2 v}\right)^{\frac{\alpha_3}{4}}\right)}{v(e_1 - e_2 v)} G_{0,\ \frac{\alpha_2}{2}+1}^{\frac{\alpha_2}{2}+1,\ 0}\left(K_2\left(\frac{v_2 - v}{c_1 - (v_2 - v)c_2}\right)^{\frac{\alpha_1\alpha_2}{4}} \middle| \begin{matrix} -, & - \\ 0, & \Delta\left(\frac{\alpha_2}{2}, s - \frac{\alpha_2(\mu_2+n)}{2}\right) \end{matrix}\right)\mathrm{d}v \end{aligned} \tag{12}$$

To the best of the authors' knowledge, the integral in (12) does not have a closed-form solution. However, in order to obtain useful insights on the system performance, it is crucial to consider a simplified performance evaluation. Therefore, using $\min(a, b) < \frac{a+b}{2}$, $P_{\text{out},2}$ can be lower-bounded as

$$\begin{aligned} P_{\text{out},2}^{\text{LB}} &= \Pr\left[\min(\gamma_{U_2}, \gamma_{U_{1\to2}}) < \frac{v_2}{2}\right] = 1 - \Pr\left[\min(\gamma_{U_2}, \gamma_{U_{1\to2}}) > \frac{v_2}{2}\right] \\ &= 1 - \Pr\left[\gamma_{U_2} > \frac{v_2}{2}\right]\Pr\left[\gamma_{U_{1\to2}} > \frac{v_2}{2}\right] = 1 - (1 - D_1)(1 - D_2), \end{aligned} \tag{13}$$

where $D_1 = \Pr\left[\gamma_{U_2} < 0.5v_2\right]$ and $D_2 = \Pr\left[\gamma_{U_{1\to2}} < 0.5v_2\right]$ can be respectively defined by

$$D_1 = \Pr\left[\gamma_{U_2} < 0.5v_2\right] = \Pr\left[Z < \frac{0.5v_2e_3}{e_1 - 0.5v_2e_2}\right] = \int_0^{\frac{0.5v_2e_3}{e_1-0.5v_2e_2}} f_Z(z)\mathrm{d}z, \tag{14}$$

$$D_2 = \Pr\left[\gamma_{U_{1\to2}} < 0.5v_2\right] = \Pr\left[X < \frac{\phi_1}{Y} + \phi_2\right] = \int_0^{\infty} f_Y(y) \int_0^{\frac{\phi_1}{y}+\phi_2} f_X(x)\mathrm{d}x\mathrm{d}y, \tag{15}$$

where $\phi_1 = \frac{0.5v_2c_4}{(c_1-0.5v_2c_2)}$ and $\phi_2 = \frac{0.5v_2c_3}{(c_1-0.5v_2c_2)}$.

Following the derivation steps drawn in Appendix B, the lower-bound OP expression can be expressed in its closed-form, as in (16), at the top of this page, with $F = \frac{e^{-\Phi_1\phi_2^{\frac{\alpha_1}{2}}}\sqrt{\frac{2}{\alpha_2}}}{(2\pi)^{\frac{\alpha_2}{4}-0.5}}\left(\frac{\Phi_1\phi_2^{\frac{\alpha_1}{2}-1}\phi_1\alpha_1}{\alpha_2}\right)^{\frac{\alpha_2(\mu_2+n)}{2}-s}$ and $K = \Phi_2\left(\frac{\Phi_1\phi_2^{\frac{\alpha_1}{2}-1}\phi_1\alpha_1}{\alpha_2}\right)^{\frac{\alpha_2}{2}}$. It is worthwhile noting that α_1 and α_2 should be even numbers. Additionally, the derivation of an asymptotic high-SNR expression for the lower-bound outage probability is shown in Appendix C.

Remark. Note that the expressions in (12), (16), (18), and (21) converge to a finite number for the summations comprising the first 20 terms for variables m_∞ and n_∞, that is, $m_\infty = n_\infty = 20$.

$$P_{\text{out},2}^{\text{LB}} = 1 - \left[1 - \sum_{m=0}^{m_\infty} \frac{(\mu_3\kappa_3)^m \gamma\left(\mu_3 + m, \Phi_3(\frac{0.5v_2e_3}{e_1-0.5v_2e_2})^{\frac{\alpha_3}{2}}\right)}{m!\Gamma(\mu_3+m)e^{\mu_3\kappa_3}}\right]$$
$$\times\left[\sum_{n=0}^{n_\infty}\sum_{m=0}^{m_\infty} \frac{A(\mu_1\kappa_1)^m}{m!e^{\mu_1\kappa_1}} \sum_{p=0}^{\mu_1+m-1} \frac{(\Phi_1)^p}{\phi_1^{-\frac{\alpha_1 p}{2}}p!} \sum_{s=0}^{\frac{\alpha_1 p}{2}} \frac{\frac{\alpha_1 p}{2}!\left(\frac{\phi_2}{\phi_1}\right)^{\frac{\alpha_1 p}{2}-s} F}{(\frac{\alpha_1 p}{2}-s)!s!} G_{0,\ \frac{\alpha_2}{2}+1}^{\frac{\alpha_2}{2}+1,\ 0}\left(K\middle|\begin{matrix}-, & -\\ 0,\ \Delta\left(\frac{\alpha_2}{2}, s-\frac{\alpha_2(\mu_2+n)}{2}\right)\end{matrix}\right)\right] \tag{16}$$

4 | ERGODIC CAPACITY

Similar to Reference 53, the ergodic capacity expression for the direct S-to-U_2 link is defined as

$$C_{\text{erg}}^{\gamma_{U_2}} = \int_0^{\infty} H_p \log_2\left(1+\gamma_{U_2}\right) f_{\gamma_{U_2}}\mathrm{d}\gamma_{U_2}. \tag{17}$$

Proposition 1. *The ergodic capacity expression related to the direct S-to-U_2 link is defined as in (18), where $E = e_1 + e_2$, $\zeta_3 = \frac{\alpha_3(\mu_3+c)}{2}$ and $D = \frac{\alpha_3\mu_3^{2c+\mu_3}\kappa_3^c(1+\kappa_3)^{c+\mu_3}}{2c!\Gamma(c+\mu_3)e^{\mu_3\kappa_3}}$. It is worthwhile noting that α_3 should be an even number.*

Proof. See Appendix D.0.1. ∎

$$C_{\text{erg}}^{\gamma_{U_2}} = \frac{H_p}{\ln(2)}\left[\sum_{c=0}^{c_\infty} D\frac{\left(\frac{e_3}{E}\right)^{\frac{\alpha_3(\mu_3+c)}{2}}\frac{2}{\alpha_3}}{(2\pi)^{\frac{\alpha_3}{2}-1}} G_{\alpha_3,\ \alpha_3+1}^{\alpha_3+1,\ \frac{\alpha_3}{2}}\left(\Phi_3\left(\frac{e_3}{E}\right)^{\frac{\alpha_3}{2}}\middle|\Delta(\tfrac{\alpha_3}{2},-\zeta_3),\ \Delta(\tfrac{\alpha_3}{2},1-\zeta_3)0,\ \Delta(\tfrac{\alpha_3}{2},-\zeta_3),\ \Delta(\tfrac{\alpha_3}{2},-\zeta_3)\right)\right.$$
$$\left.-\sum_{c=0}^{c_\infty} D\frac{\left(\frac{e_3}{e_2}\right)^{\frac{\alpha_3(\mu_3+c)}{2}}\frac{2}{\alpha_3}}{(2\pi)^{\frac{\alpha_3}{2}-1}} G_{\alpha_3,\ \alpha_3+1}^{\alpha_3+1,\ \frac{\alpha_3}{2}}\left(\Phi_3\left(\frac{e_3}{e_2}\right)^{\frac{\alpha_3}{2}}\middle|\begin{matrix}\Delta\left(\frac{\alpha_3}{2},-\zeta_3\right),\ \Delta\left(\frac{\alpha_3}{2},1-\zeta_3\right)\\ 0,\ \Delta\left(\frac{\alpha_3}{2},-\zeta_3\right),\ \Delta\left(\frac{\alpha_3}{2},-\zeta_3\right)\end{matrix}\right)\right] \tag{18}$$

Similarly, the general ergodic capacity expression for the U_1-to-U_2 link is

$$C_{\text{erg}}^{\gamma_{U_{1\to2}}} = \int_0^{\infty} H_p \log_2\left(1+\gamma_{U_{1\to2}}\right) f_{\gamma_{U_{1\to2}}}\mathrm{d}\gamma_{U_{1\to2}}. \tag{19}$$

Due to the complexity an exact SINDR of the U_1-to-U_2 link, the ergodic capacity evaluation is infeasible. Thus, the following approximation is applied to as follows

$$\gamma_{U_{1\to 2}} = \frac{c_1 XY}{Yc_3\left(\frac{c_2}{c_3}X+1\right)+c_4} \approx \frac{c_1 XY}{c_2 XY + c_4}, \tag{20}$$

where $c_3 \to 0$ due to the high-SNR regime.

Proposition 2. *For the U_1-to-U_2 link, the ergodic capacity expression can be expressed as in (21), where $c_5 = c_1 + c_2$, $B = \frac{\alpha_1 \mu_1^{2m+\mu_1} \kappa_1^m (1+\kappa_1)^{m+\mu_1}}{2m!\Gamma(m+\mu_1)e^{\mu_1\kappa_1}}$, $\xi = \frac{\alpha(\mu_2+n+\mu_1+m)}{4}$, $\Lambda = \frac{4}{\alpha}\left(\frac{\Phi_1}{\Phi_2}\right)^{\frac{\mu_2+n-(\mu_1+m)}{2}}$, and $\beta = \frac{\alpha(\mu_2+n+\mu_1+m)}{4}$. It is worthwhile noting that $\alpha = \alpha_1 = \alpha_2$ should be an even number.*

Proof. See Appendix D.0.2. ∎

$$C_{\text{erg},Apr}^{\gamma_{U_{1\to 2}}} = \frac{H_p}{\ln(2)}\left[\sum_{m=0}^{m_\infty} B \sum_{n=0}^{n_\infty} A\Lambda \frac{\left(\frac{c_4}{c_5}\right)^\beta}{\alpha(2\pi)^{\frac{\alpha}{2}-1}} G_{\alpha,\ \alpha+2}^{\alpha+2,\ \frac{\alpha}{2}}\left(\Phi_1\Phi_2\left(\frac{c_4}{c_5}\right)^{\frac{\alpha}{2}}\middle|\begin{matrix}\Delta(\frac{\alpha}{2},-\xi),\ \Delta(\frac{\alpha}{2},1-\xi)\\ \frac{\mu_2+n-(\mu_1+m)}{2},\ \frac{\mu_1+m-(\mu_2+n)}{2},\ \Delta(\frac{\alpha}{2},-\xi),\ \Delta(\frac{\alpha}{2},-\xi)\end{matrix}\right)\right.$$
$$\left. - \sum_{m=0}^{m_\infty} B \sum_{n=0}^{n_\infty} A\Lambda \frac{\left(\frac{c_4}{c_2}\right)^\beta}{\alpha(2\pi)^{\frac{\alpha}{2}-1}} G_{\alpha,\ \alpha+2}^{\alpha+2,\ \frac{\alpha}{2}}\left(\Phi_1\Phi_2\left(\frac{c_4}{c_2}\right)^{\frac{\alpha}{2}}\middle|\begin{matrix}\Delta(\frac{\alpha}{2},-\xi),\ \Delta(\frac{\alpha}{2},1-\xi)\\ \frac{\mu_2+n-(\mu_1+m)}{2},\ \frac{\mu_1+m-(\mu_2+n)}{2},\ \Delta(\frac{\alpha}{2},-\xi),\ \Delta(\frac{\alpha}{2},-\xi)\end{matrix}\right)\right] \tag{21}$$

Hence, U_2 achieves the total ergodic capacity that can be calcaluated as

$$C_{\text{erg}}^{U_2} = C_{\text{erg}}^{\gamma_{U_{1\to 2}}} + C_{\text{erg}}^{\gamma_{U_2}}. \tag{22}$$

5 | RESULTS DISCUSSION

In this section, we quantify the performance of the considered system model with imperfect hardware over a generalized $\alpha-\kappa-\mu$ fading model. We assume that the system parameters (which mainly follow the works[54-56]) are defined as in Table 3[§], unless stated otherwise.

Note that the analytical findings for the lower-bound outage probability are discussed and supported by thorough Monte-Carlo simulation,[18,24] with 10^7 iterations.

Figure 2 presents the ergodic capacity results vs the energy harvesting factors ρ/η at the transmit SNR of 50 dB. When the EH-aimed amount of power is too small or too much, the capacity metric deteriorates. From the plot, one can deduce that $\eta = 0.07$ and $\rho = 0.91$ are optimal values for the TSR and PSR protocols, respectively. These factors keep being valid for a range of cases with different external conditions. Thus, the aforementioned values of ρ and η are used in all the next simulation results.

Figure 3 illustrates some results on the PSR-based outage probability of U_2 over Weibull and Rayleigh fading channels for the OMA and NOMA scenarios, when $\mathfrak{d} = 0.2$. It includes the Monte-Carlo simulation results for the exact and lower-bounded outage probabilities, where, at the high-SNR values, the lower-bound OP curves tend towards the exact OP. For example, considering the Rayleigh ($\alpha = 2$, $\kappa = 0$, $\mu = 1$) fading channels, the OP of 10^{-1} can be obtained at the transmit SNR values of 30 and 39 dB for the exact and lower-bound OP curves, respectively. However, the OP of 10^{-3} is

TABLE 3 System parameters

Distances, m	**EH efficiency, ϖ**	**PSR factor, ρ**	**Path-loss exponent, τ**
$d_1 = 2.1, d_2 = 1.1, d_3 = 3.1$	0.8	0.91	2.7
PA coefficients	**HI levels' range, $\mathfrak{d}$**	**TSR factor, η**	**Rate threshold, ν, dB**
$a_1 = 0.2, a_2 = 0.8$	$\{0.05, 0.15\}$	0.07	3

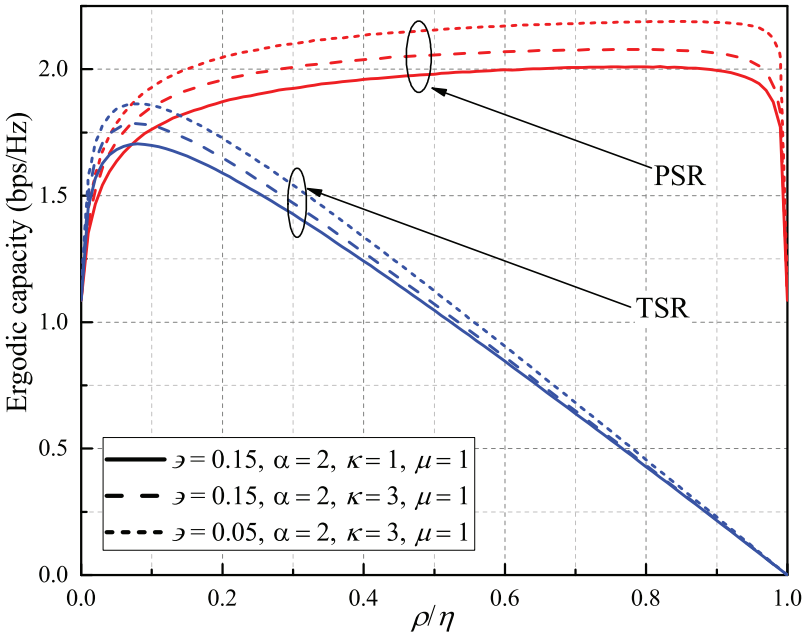

FIGURE 2 The ergodic capacity vs ρ/η for the PSR and TSR at the transmit SNR of 50 dB for various ∋

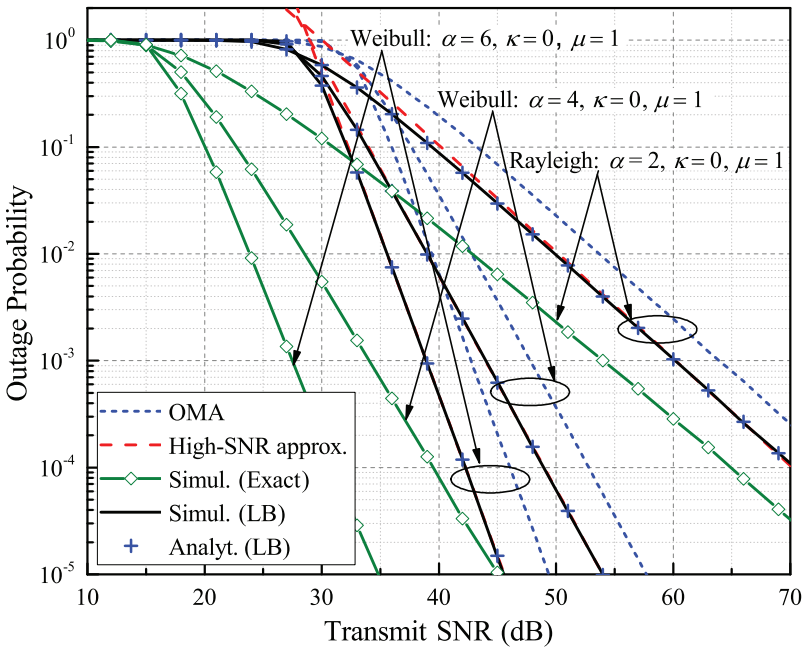

FIGURE 3 The outage probability vs the transmit SNR for the OMA, NOMA and high-SNR cases, when ∋ = 0.2

reached at the transmit SNR values of 54 and 60 dB for the exact and lower-bound OP simulation results, respectively. The proposed NOMA network scenario aims at delivering desired information to designated receivers over two time slots; however, its OMA counterpart needs to allocate three time slots. Having this in mind, Figure 3 demonstrates a noticeable difference in the OP results for the NOMA and OMA cases over all considered fading types. The OMA-based results, in general, are characterized by the worse performance. Moreover, one can observe that the high-SNR approximated OP curves are in good agreement with the OP results. Figure 3 supports the claim mentioned earlier, that increasing α parameter improves the outage performance. This becomes apparent through a comparison of the results for the exact and

lower-bound OP over Rayleigh ($\alpha = 2$, $\kappa = 0$, $\mu = 1$) and Weibull ($\alpha = 4$ and $\alpha = 6$, $\kappa = 0$, $\mu = 1$) channels. Note that the lower-bound OP curves change in a similar pattern as the exact ones as α changes.

Similarly, Figure 4 shows the outage probability of U_2 under low and high HI levels over the generalized fading model. The analytical results are in good match with the Monte-Carlo ones. Such an observation successfully validates the analytical findings. Generally, the performance degradation is noticed for all channel realizations as the HI degree increases. It is important to note that the HI effect is more harsh, when the fading parameters α, κ, and μ increase. It implies the stronger correlation between the OP performance degradation and increase in HIs for the PSR rather than for the TSR. Additionally, the optimal protocol in terms of better outage probability performance changes over a range of parameters

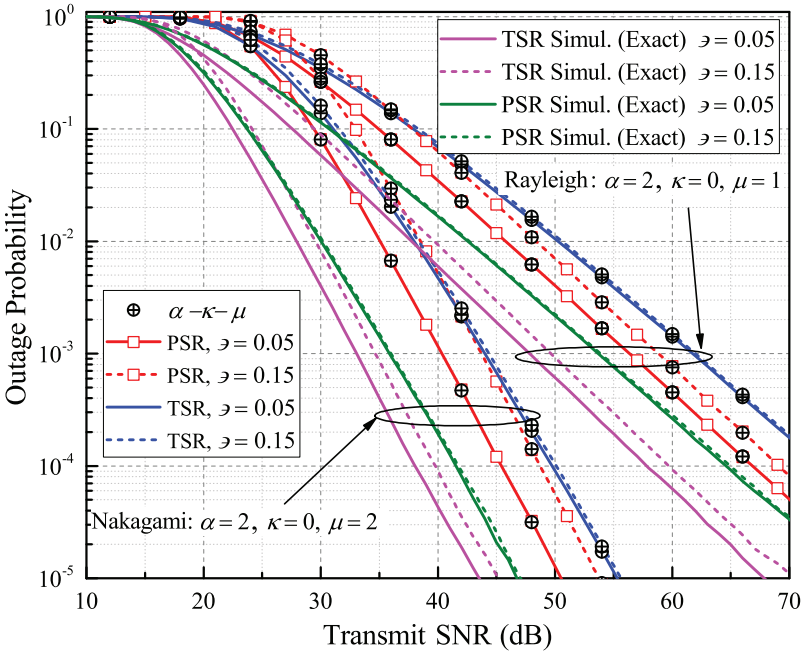

FIGURE 4 The outage probability vs the transmit SNR, when $\vartheta = \{0.05, 0.15\}$

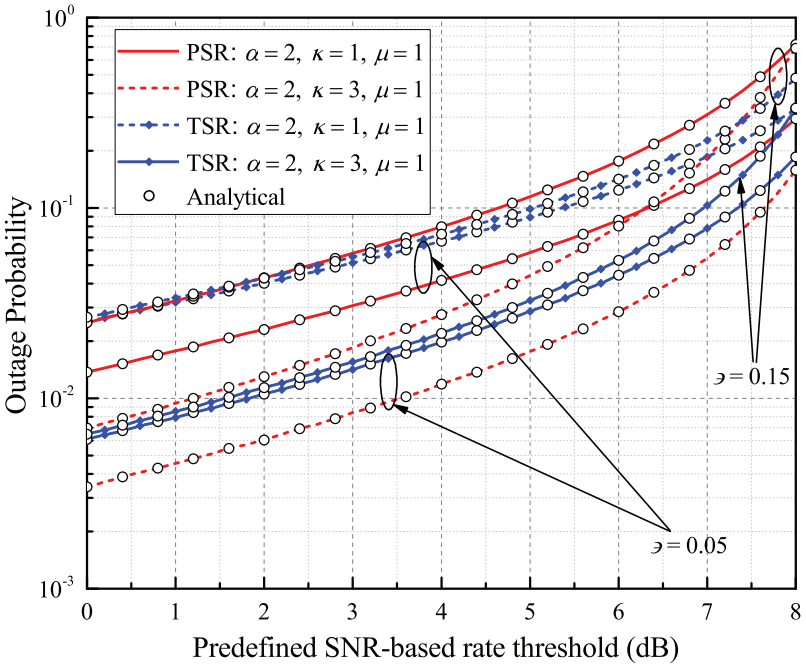

FIGURE 5 The outage probability vs the SNR-associated rate threshold at the transmit SNR of 39 dB, when $\vartheta = \{0.05, 0.15\}$

such as the channel conditions, HIs level, and the transmit SNR. For example, at a low HI level ($\mathfrak{d} = 0.05$), the PSR is superior over the whole transmit SNR range and channel conditions. However, when a high HI level ($\mathfrak{d} = 0.15$) is introduced, the TSR shows better performance up to 35 and 40 dB of the transmit SNR under Rayleigh and Nakagami-m channel fading models, respectively.

Figure 5 depicts the outage probability at the transmit SNR of 39 dB vs the pre-defined rate threshold for different fading models and under the PSR and TSR protocols. The increase of HI is noticed to have a more severe impact on the outage probability under the PSR protocol than the TSR. Although the considered network's performance is better under the PSR protocol at a low HIs level, the TSR illustrates a superior performance at a high HIs level. For clarity purposes, the values of parameters α and μ are left unchanged and κ is intentionally chosen to have different values. For both PSR and TSR, increasing κ parameter improves the outage probability. Overall, as it is expected, the outage performance degrades as the pre-defined SNR-based rate threshold goes up.

Figure 6 demonstrates the outage probability under different parameters of HIs levels and μ for generalized fading model over the TSR protocol. Interestingly, the figure shows that the increase in the HI level has a different effect on the performance concerning the channel conditions. For example, the outage probability degradation due to the increase of HI from 0.05 to 0.15, is more severe at $\mu = 4$ than at $\mu = 2$. Moreover, the change of μ has a different effect on the performance. When the number of multipaths changes from $\mu = 4$ to $\mu = 3$, the degradation of the outage probability is less in comparison with the change from $\mu = 3$ to $\mu = 2$. The results suggest that μ has a more considerable impact on the outage probability rather than $\mathfrak{d}$. Increasing the μ decreases the outage probability due to the availability of multiple signal replicas at the receiver site. However, at the transmit SNR up to 25 dB, the outage probability at $\mathfrak{d} = 0.05$ and $\mu = 3$ is better than that at $\mathfrak{d} = 0.15$ and $\mu = 4$.

Next, in Figure 7, we demonstrate the outage results achievable by U_1 (the only user that performs SIC) built vs a SIC error factor for the PSR and TSR protocols. The transmit SNR is fixed at 45 dB. Once can observe that the perfect hardware scenario, that is, $\varsigma = 0$, reveals that the TSR outperforms its considered counterpart and it lasts up to approx. $\varsigma = 0.2$. At this intersection point, the PSR starts prevailing and the corresponding performance deterioration rate is lower than the one of the TSR. On the other hand, for the scenarios of compounded hardware and SIC impairments, it is apparent that this intersection happens at lower SIC error factors, as expected. This observation shows that, at low SIC region, it is more reasonable to deploy the TSR protocol if extreme low outage performance is required. However, if such requirement is not mandatory, then it is more appropriate to exploit the PSR protocol as it provides more robust performance degradation, that is, the outage slope rate is relatively lower.

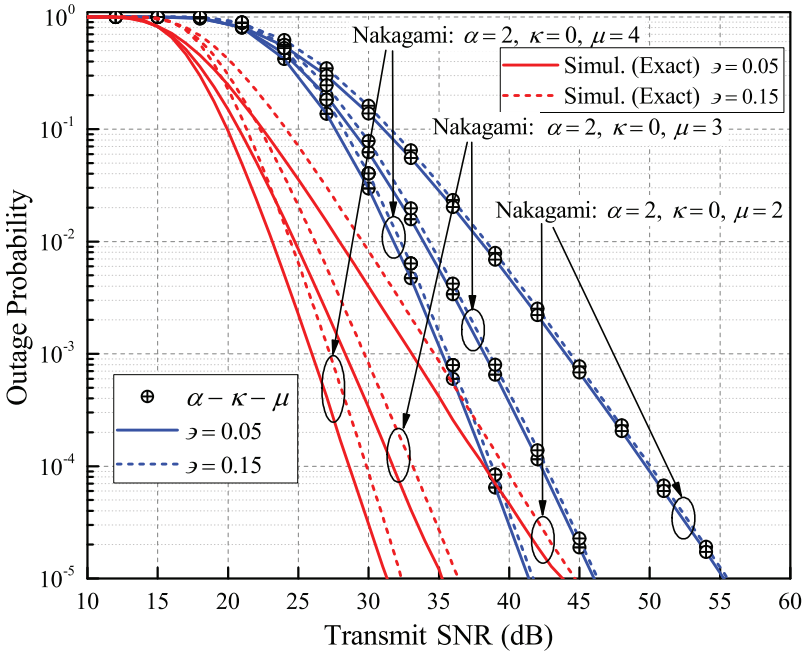

FIGURE 6 The outage probability vs the transmit SNR for the TSR protocol with various μ and $\mathfrak{d}$ parameters

Figure 8 plots the average throughput vs the transmit SNR at $\nu = 3$ dB. Similar to the outage probability, the throughput degrades when ϶ increases. Due to the considered system model and NOMA concept, the throughput saturates for all network scenarios. For comparison purposes, the values of ϶ = {0.05, 0.1, 0.15} are considered for the PSR and TSR protocols to evaluate the throughput over Rayleigh channels. The results suggest that increasing the HI level decreases the average throughput at the same rate for both protocols. Overall, the optimal protocol in terms of higher throughput characteristics varies over a range of HI values. For example, the TSR protocol is preferred at the transmit SNR of up to 22, 27, and 32 dB for the HI levels of 0.05, 0.1, and 0.15, respectively. Otherwise, the PSR protocol shows higher average

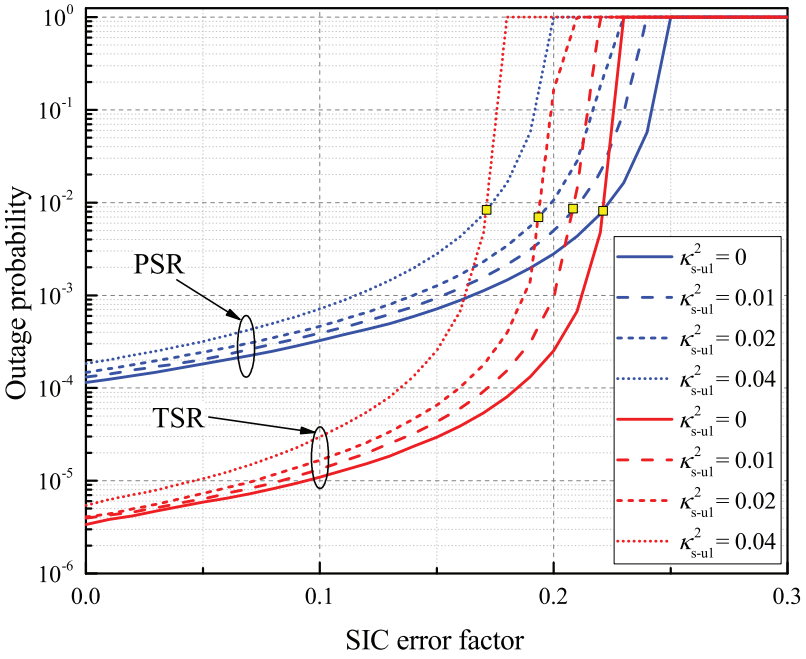

FIGURE 7 The outage performance of U_1 vs the SIC error factor, when the transmit SNR equals 45 dB

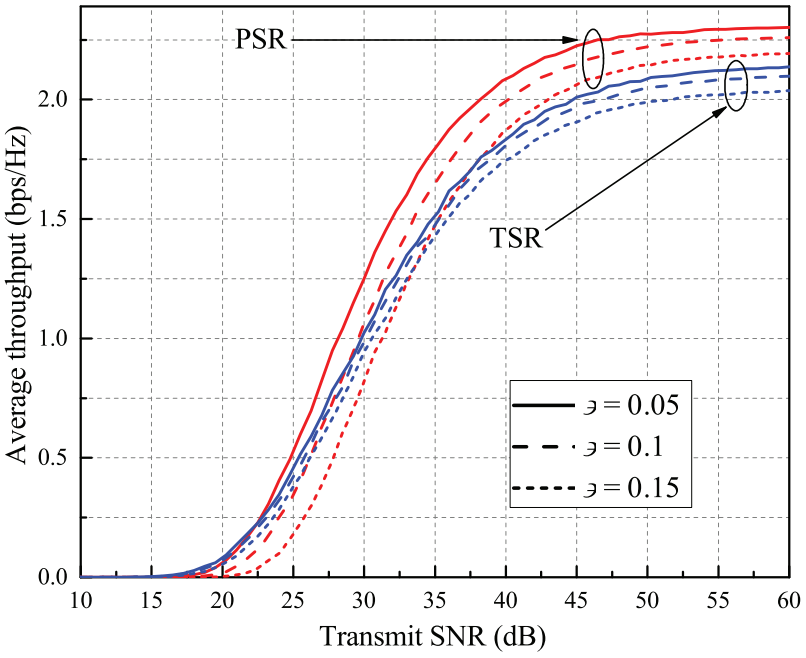

FIGURE 8 The average throughput vs the transmit SNR, when ϶ = {0.05, 0.1, 0.15}

throughput. The minimum throughput saturation of around 2.2 and 2.05 bps/Hz are observed at ϶ = 0.15 for the PSR and TSR, respectively. Simultaneously, the throughput at low HIs saturates at around 2.35 and 2.15 bps/Hz for the PSR and TSR, accordingly. Due to the NOMA constraints, after certain transmit SNR, the effect of interference in (3) and (8) starts to fade, while the increase in the transmit SNR becomes less influential. As a result, the saturation happens as these expressions start depending on $\frac{b_1}{b_2}$ and $\frac{c_1}{c_2}$, accordingly.

Figure 9 shows the ergodic capacity for different channel conditions over both protocols and low HI cases. For the entire range of transmit SNR and corresponding channel conditions, the PSR protocol demonstrates better performance than the TSR. Increasing μ improves both protocols' overall performance while having a more significant effect on the increase of the ergodic capacity for the TSR. The NOMA constraints can explain both protocols' performance saturation, where the PSR and TSR scenarios saturate at around 2.3 and 2.16 bps/Hz, respectively. The investigation of the results suggests that the applied approximation works better for the TSR protocol case rather than the PSR as the results for the TSR closely follow the simulation.

Similarly, Figure 10 demonstrates the impact various HI quality levels on the average capacity over Rayleigh fading. For both protocols, the capacity performance degrades as the HI quality reduces. Overall, the ergodic capacity performance degrades more severely due to HIs under the PSR protocol. Interestingly, the effect of increasing HIs level on capacity is more significant at the high SNR values. Additionally, for comparison purposes, the capacity plots are shown for the OMA system as well, illustrating the better performance of the NOMA up to 30 dB under the PSR protocol. The effect of interference in (3) and (8) starts decreasing after a certain transmit SNR is reached. Therefore, the saturation happens as these expressions start to depend on $\frac{b_1}{b_2}$ and $\frac{c_1}{c_2}$, accordingly. In essence, the saturation starts at 30 dB for all NOMA cases under various HI levels.

Figure 11 evaluates the impact of HI levels and channel conditions on the ergodic capacity vs the transmit SNR. Overall, the asymptotic results closely follow the simulation over the whole range of ϶ and $\alpha - \kappa - \mu$ parameter combinations. All cases start saturating at 30 dB due to the NOMA's constraints, and reach 2.3 and 2.25 bps/Hz for ϶ = 0.05 and ϶ = 0.1 scenarios, respectively. Unlike the HI at transceivers, better channel conditions do not affect the saturation level of the ergodic capacity. For example, when ϶ = 0.05 is considered, the ergodic capacity ceiling for scenarios with $\alpha = 4$, $\kappa = 0$, $\mu = 1$ and $\alpha = 2$, $\kappa = 0$, $\mu = 1$ is the same. On the other hand, for the case with identical channel conditions ($\alpha = 2$, $\kappa = 0$, $\mu = 1$) and different HIs level (϶ = 0.05 and ϶ = 0.1), the ergodic capacity ceiling changes from 2.3 to 2.25 bps/Hz, accordingly.

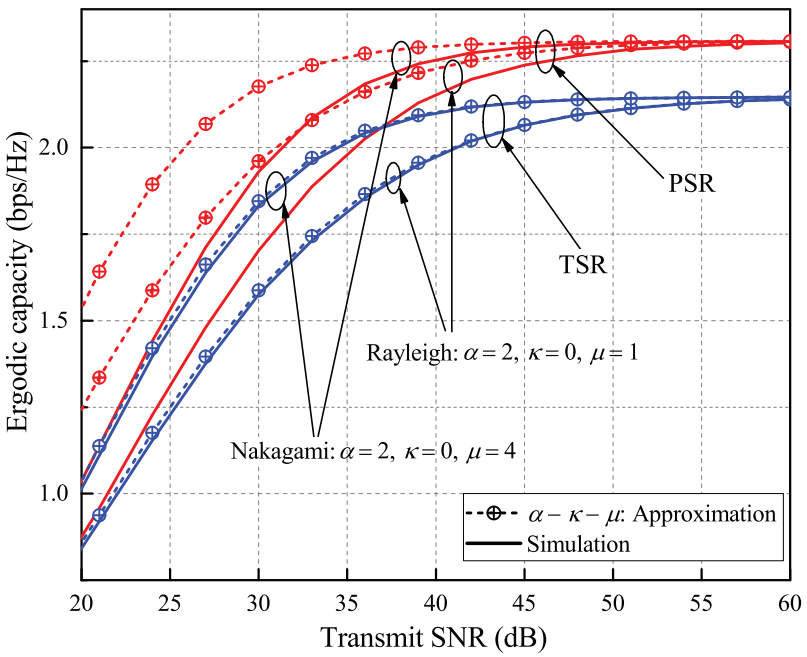

FIGURE 9 Ergodic capacity: the simulation and approximation results for the PSR ($\rho = 0.91$) and TSR ($\eta = 0.07$) protocols, when ϶ = 0.05

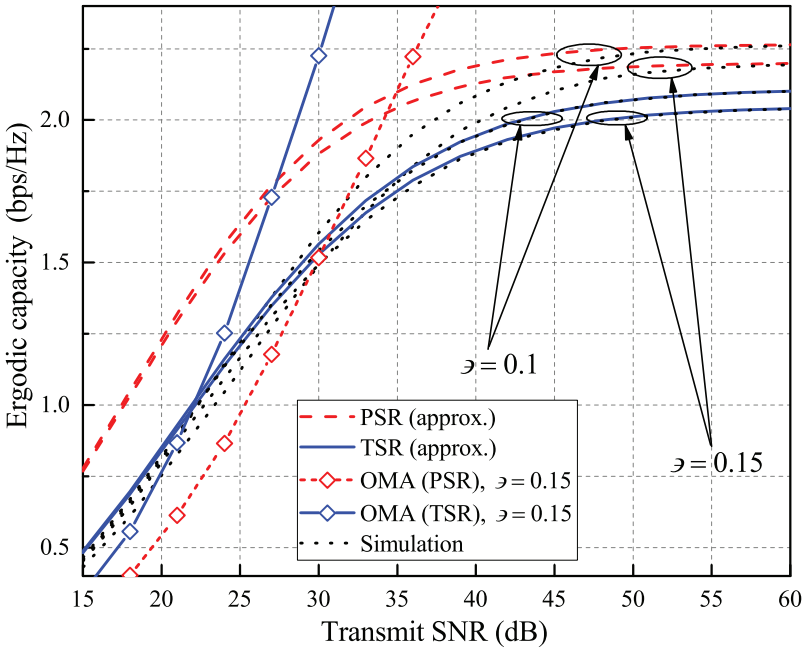

FIGURE 10 The ergodic capacity for the PSR ($\rho = 0.91$) and TSR ($\eta = 0.07$) protocols under OMA and NOMA schemes, when ϶ = {0.1, 0.15}

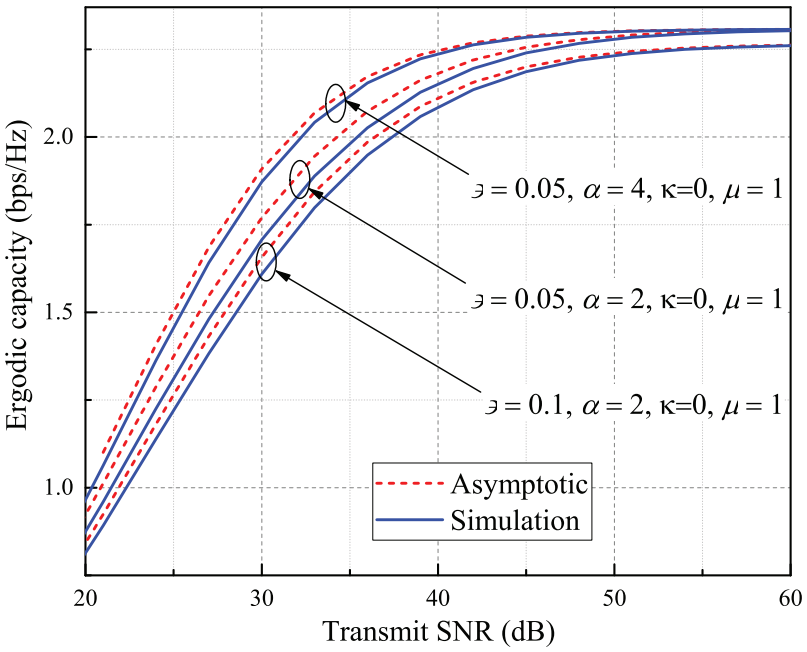

FIGURE 11 The asymptotic values of ergodic capacity for the PSR ($\rho = 0.91$) protocol under different α and ϶ parameters

For the two-hop cooperative NOMA architecture, the ergodic capacity saturates and there is no need to increase the transmit SNR after a certain point. For such network the ergodic capacity starts degrading more severely when the transmit SNR grows. Additionally, the boundary values of the transmit SNR for the NOMA system to outperform its OMA counterpart in terms of ergodic capacity differ with respect to the energy harvesting protocol. After reaching these boundary levels, the OMA system becomes more favorable. Overall, the capacity saturation for two-hop cooperative NOMA under consideration starts at 30 dB for all the NOMA cases under any HIs level and channel fluctuations. The ergodic capacity ceiling is affected by the HIs level at transceivers, while the change of channel conditions does not affect it.

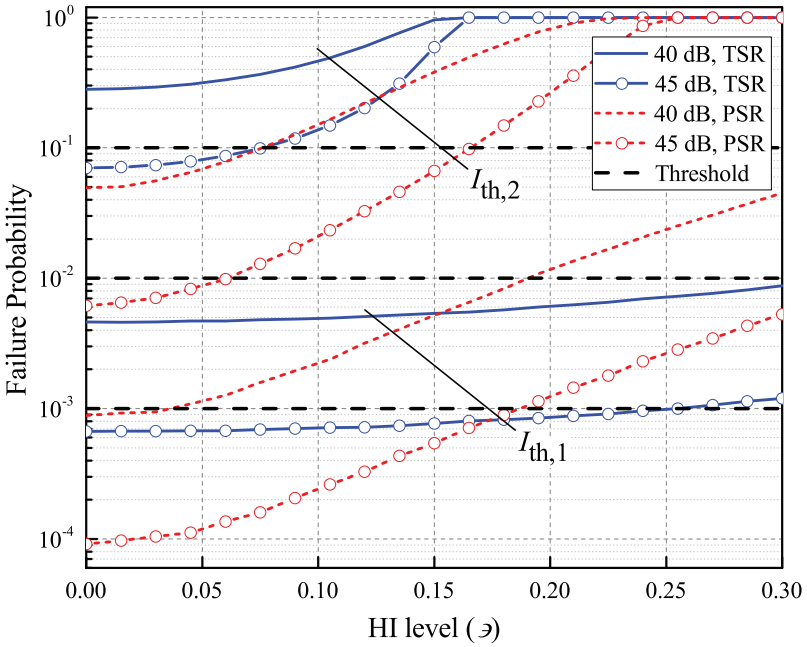

FIGURE 12 The failure probability for the PSR and TSR protocols for different values of ə

Figure 12 shows the failure probability for both protocols with respect to the HI levels and transmit SNR under Nakagami-m ($\alpha = 2$, $\kappa = 0$, $\mu = 2$) fading. The failure occurs when the achieved data rate falls below the predefined threshold, defined as $\mathcal{I}_{\text{th}}$. The data rate threshold values of $\mathcal{I}_{\text{th},1}$ and $\mathcal{I}_{\text{th},2}$ are equal to 0.8 and 1.4 bps/Hz, accordingly. We consider the failure threshold levels of 10^{-1}, 10^{-2}, 10^{-3} for three different systems and the transmit SNR values of 40 and 45 dB. Overall, the observed increase in the failure probability occurs with a higher HIs and data rate threshold level. The system with $\mathcal{I}_{\text{th},1}$ data rate threshold and the transmit SNR of 40 dB, experiences the failure and approaches the failure threshold of 10^{-3} even at low HI levels, under the TSR and PSR protocols, accordingly. Furthermore, the system under the same conditions and the transmit SNR of 45 dB shows higher tolerance for the increase in the HI level under both protocols, where failure occurs at ə values of 0.18 and 0.23 for both protocols, respectively.

Unlike the scenario with $\mathcal{I}_{\text{th},2}$, the failure probability of the network under the TSR protocol and $\mathcal{I}_{\text{th},1}$ is less susceptible to the changes in HI levels. Whereas, for the TSR-enabled network with $\mathcal{I}_{\text{th},2}$, the failure happens at ə values of 0.15 and 0.16 for 40 and 45 dB of transmit SNR, accordingly. In contrast, the PSR protocol's failure probability has a significant relationship with ə for both data rate thresholds. For example, the failure probability degrades by almost ten times for both transmit SNR levels, while the HIs level ranges between the ideal case and 0.2 at $\mathcal{I}_{\text{th},1}$. In comparison with PSR, the failure happens at lower levels of ə for TSR at $\mathcal{I}_{\text{th},2}$. Additionally, at a certain transmit SNR level, the optimal energy harvesting protocol in terms of failure probability changes depending on the level of HIs level. For example, the case with a PSR protocol and $\mathcal{I}_{\text{th},1}$ remains the optimal one only up to ə values of 0.15 and 0.17 for the transmit SNR of 40 and 45 dB, respectively.

Depending on the required outage level requirements and inter-node distance values, there are certain transmit SNR values chosen at the base station of the considered two-hop cooperative NOMA architecture. At this transmit SNR value, it is essential to choose the optimal energy harvesting protocol, because at a certain transmit SNR, it would be better either to choose the PSR protocol and spend resources on equipment with a lower HIs level or choose the TSR protocol without any additional investment. Moreover, if the PSR protocol is used, the channel degradation, for example, decreasing the number of multipath clusters can be compensated by investing in transceivers with a lower HI level. However, such trade-off cannot be implemented for the TSR protocol.

6 | CONCLUSION

This work contributes to the field of performance analysis of wireless powered cooperative NOMA subject to the hardware imperfections. We derived the expressions for the outage probability and ergodic capacity metrics over a generalized

$\alpha - \kappa - \mu$ fading model, which special cases are the Weibull, Rician and so forth. The analytical OP expressions were analyzed over a number of HI levels and demonstrated the consistency over a $\alpha - \kappa - \mu$ statistical model, and were further validated by Monte-Carlo simulations for both protocols. The approximate and asymptotic ergodic capacity expressions were obtained and investigated for the TSR and PSR protocols. Finally, the results underlined the importance of considering the hardware imperfections existing at the transceivers' front-ends for the applications with strict reliability conditions. Finally, the results suggested that the HI impact on OP enhances, when the parameters α, κ, and μ increase.

ACKNOWLEDGMENT

Nazarbayev University Social Policy Grant and the Nazarbayev University Faculty Development Competitive Research Program under Grant no. 240919FD3935.

CONFLICT OF INTEREST

The authors declare no potential conflict of interest.

DATA AVAILABILITY STATEMENT

The data that support the findings of this study are available from the corresponding author upon reasonable request.

ENDNOTES

*It is important to highlight that, for the outage performance, the considered system model is non-homogeneous allowing each individual link to follow different statistical models.

†This statistical model is considered to be general as it includes the other fading models,[44,48,49] for example, Weibull, Rice and so forth

‡Note that, in this article, unlike Reference 51, we consider a linear energy harvesting model to facilitate the analysis, when ϖ is independent of the input power level of an EH circuitry. Non-linear ϖ modeling imposes resource optimization problems which are beyond the scope of this article.

§We assume that the QoS of U_1 is satisfied due to its proximity to S.

ORCID

Galymzhan Nauryzbayev https://orcid.org/0000-0003-4470-3851

REFERENCES

1. Khan LU, Yaqoob I, Imran M, Han Z, Hong CS. 6G wireless systems: a vision, architectural elements, and future directions. *IEEE Access*. 2020;8:147029-147044.
2. Xiao M, Mumtaz S, Huang Y, et al. Millimeter wave communications for future mobile networks. *IEEE J Select Areas Commun*. 2017;35(9):1909-1935.
3. Akyildiz IF, Han C, Nie S. Combating the distance problem in the millimeter wave and terahertz frequency bands. *IEEE Commun Mag*. 2018;56(6):102-108.
4. Shan H, Zhuang W, Wang Z. Distributed cooperative MAC for multihop wireless networks. *IEEE Commun Mag*. 2009;47(2):126-133.
5. Cisco. Annual internet report 2018-2023 (white paper): CISCO; 2020.
6. Arzykulov S, Nauryzbayev G, Tsiftsis TA, Maham B, Hashmi MS, Rabie KM. Underlay spectrum sharing for NOMA relaying networks: outage analysis. Proceedings of the 2020 International Conference on Computing, Networking and Communications (ICNC); February 17–20, 2020:897-901; Big Island, HI.
7. Nauryzbayev G, Arzykulov S, Tsiftsis TA, Abdallah M. Performance of cooperative underlay CR-NOMA networks over Nakagami-M channels. Proceedings of the 2018 IEEE International Conference on Communications Workshops (ICC Workshops); 2018:1-6.
8. Ding Z, Yang Z, Fan P, Poor HV. On the performance of non-orthogonal multiple access in 5G systems with randomly deployed users. *IEEE Signal Process Lett*. 2014;21(12):1501-1505.
9. Liang X, Wu Y, Ng DWK, Zuo Y, Jin S, Zhu H. Outage performance for cooperative NOMA transmission with an AF relay. *IEEE Commun Lett*. 2017;21(11):2428-2431.
10. Men J, Ge J, Zhang C. Performance analysis of nonorthogonal multiple access for relaying networks over nakagami-*m* fading channels. *IEEE Trans Veh Technol*. 2017;66(2):1200-1208.
11. Zhang L, Liu J, Xiao M, Wu G, Liang Y-C, Li S. Performance analysis and optimization in downlink NOMA systems with cooperative full-duplex relaying. *IEEE J Select Areas Commun*. 2017;35(10):2398-2412.
12. Nikopour H, Baligh H. Sparse code multiple access. Proceedings of the 2013 IEEE 24th Annual International Symposium on Personal, Indoor, and Mobile Radio Communications (PIMRC); 2013:332-336; IEEE.
13. Ding Z, Liu Y, Choi J, et al. Application of non-orthogonal multiple access in LTE and 5G networks. *IEEE Commun Mag*. 2017;55(2):185-191.
14. Farhadi ZA, Bakhshi H. Resource allocation in sparse code multiple access-based systems for cloud-radio access network in 5G networks. *Trans Emerg Telecommun Technol*. 2021;32(1):e4153.

15. Farhadi ZA, Bakhshi H. Three-step optimization algorithm in SCMA-based system for user association and resource allocation in C-RAN. *Int J Inf Commun Technol Res*. 2020;12:11-21.
16. Dai L, Wang B, Yuan Y, Han S, Chih-lin I, Wang Z. Non-orthogonal multiple access for 5G: solutions, challenges, opportunities, and future research trends. *IEEE Commun Mag*. 2015;53(9):74-81.
17. Nosratinia A, Hunter TE, Hedayat A. Cooperative communication in wireless networks. *IEEE Commun Mag*. 2004;42(10):74-80.
18. Ding Z, Peng M, Poor HV. Cooperative non-orthogonal multiple access in 5G systems. *IEEE Commun Lett*. 2015;19(8):1462-1465.
19. Liu Y, Ding Z, Elkashlan M, Poor HV. Cooperative non-orthogonal multiple access with simultaneous wireless information and power transfer. *IEEE J Select Areas Commun*. 2016;34(4):938-953.
20. Varshney LR. Transporting information and energy simultaneously. Proceedings of the 2008 IEEE International Symposium on Information Theory; 6–11 July 2008:1612-1616.
21. Xu Y, Shen C, Ding Z, et al. Joint beamforming and power-splitting control in downlink cooperative SWIPT NOMA systems. *IEEE Trans Signal Process*. 2017;65(18):4874-4886.
22. Zhou F, Li Z, Cheng J, Li Q, Si J. Robust AN-aided beamforming and power splitting design for secure MISO cognitive radio with SWIPT. *IEEE Trans Wirel Commun*. 2017;16(4):2450-2464.
23. Nasir AA, Zhou X, Durrani S, Kennedy RA. Relaying protocols for wireless energy harvesting and information processing. *IEEE Trans Wirel Commun*. 2013;12(7):3622-3636.
24. Yang Z, Ding Z, Fan P, Al-Dhahir N. The impact of power allocation on cooperative non-orthogonal multiple access networks with SWIPT. *IEEE Trans Wirel Commun*. 2017;16(7):4332-4343.
25. Akki AS, Haber F. A statistical model of mobile-to-mobile land communication channel. *IEEE Trans Veh Technol*. 1986;35(1):2-7.
26. Johansson NA, Wang YPE, Eriksson E, Hessler M. Radio access for ultra-reliable and low-latency 5G communications. Proceedings of the 2015 IEEE International Conference on Communication Workshop (ICCW); 8-12 June 2015:1184-1189.
27. Nauryzbayev G, Abdallah M, Ansari IS, Al-Dhahir N, Qaraqe K. Outage of cognitive electric vehicle networks over mixed RF/VLC channels with signal-dependent noise and imperfect CSI. *IEEE Trans Veh Technol*. 2020;69(6):6828-6832.
28. Nauryzbayev G, Abdallah M, Elgala H. Outage of SEE-OFDM VLC-NOMA networks. *IEEE Photon Technol Lett*. 2019;31(2):121-124.
29. Pan G, Ye J, Ding Z. Secure hybrid VLC-RF systems with light energy harvesting. *IEEE Trans Commun*. 2017;65(10):4348-4359.
30. Shepherd NH. Coverage prediction for mobile radio systems operating in the 800/900 MHz frequency range. *IEEE Trans Veh Technol*. 1988;37(1):3-72.
31. Wu Q, Matolak DW, Sen I. 5-GHz-band vehicle-to-vehicle channels: models for multiple values of channel bandwidth. *IEEE Trans Veh Technol*. 2010;59(5):2620-2625.
32. Bai T, Heath RW. Coverage and rate analysis for millimeter-wave cellular networks. *IEEE Trans Wirel Commun*. 2015;14(2):1100-1114.
33. Schenk T. *RF Imperfections in High-rate Wireless Systems: Impact and Digital Compensation*. New York, NY: Springer; 2008.
34. Björnson E, Hoydis J, Kountouris M, Debbah M. Massive MIMO systems with non-ideal hardware: energy efficiency, estimation, and capacity limits. *IEEE Trans Inf Theory*. 2014;60(11):7112-7139.
35. Bjornson E, Matthaiou M, Debbah M. A new look at dual-hop relaying: performance limits with hardware impairments. *IEEE Trans Commun*. 2013;61(11):4512-4525.
36. Qi J, Aissa S, Alouini M-S. Dual-hop amplify-and-forward cooperative relaying in the presence of Tx and Rx in-phase and quadrature-phase imbalance. *IET Commun*. 2014;8(3):287-298.
37. Li J, Matthaiou M, Svensson T. I/Q imbalance in AF dual-hop relaying: performance analysis in Nakagami−*m* fading. *IEEE Trans Commun*. 2014;62(3):836-847.
38. Björnson E, Papadogiannis A, Matthaiou M, Debbah M. On the impact of transceiver impairments on AF relaying. Proceedings of the 2013 IEEE International Conference on Acoustics, Speech and Signal Processing; 2013:4948-4952; Vancouver, BC, Canada.
39. Reshma K, Babu AV. Cooperative NOMA system with incremental relaying and energy harvesting: performance analysis and optimization. *Trans Emerg Telecommun Technol*. 2020;31(9):e4075.
40. Al-Amin A, Young SS. Performance analysis of cooperative nonorthogonal multiple access with improved time switching simultaneous wireless information and power transfer protocol. *Trans Emerg Telecommun Technol*. 2020;31(11):e4077.
41. Li X, Li J, Li L. Performance analysis of impaired SWIPT NOMA relaying networks over imperfect Weibull channels. *IEEE Syst J*. 2020;14(1):669-672.
42. Kader MF, Uddin MB, Islam A, Shin SY. Cooperative non-orthogonal multiple access with SWIPT over Nakagami-m fading channels. *Trans Emerg Telecommun Technol*. 2019;30(5):e3571.
43. Kumar V, Cardiff B, Flanagan MF. Performance analysis of NOMA-based cooperative relaying in α-μ fading channels. Proceedings of the 2019 IEEE International Conference on Communications (ICC); 2019:1-7; Shanghai, China.
44. Arzykulov S, Nauryzbayev G, Hashmi MS, Eltawil AM, Rabie KM, Seilov S. Hardware- and interference-limited cognitive IoT relaying NOMA networks with imperfect SIC over generalized non-homogeneous fading channels. *IEEE Access*. 2020;8:72942-72956.
45. Alqahtani AS, Alsu sa E. Performance analysis of downlink NOMA system over α-η-μ generalized fading channel. Proceedings of the 2020 IEEE 91st Vehicular Technology Conference (VTC2020-Spring); 2020:1-5; Antwerp, Belgium.
46. Gradshteyn IS, Ryzhik IM. *Table of Integrals, Series, and Products*. 7th ed. Amsterdam, The Netherlands: Elsevier; 2007.

47. Adamchik VS, Marichev OI. The algorithm for calculating integrals of hypergeometric type functions and its realization in REDUCE system. Proceedings of the 1990 International Symposium on Symbolic and Algebraic Computation; August 2020:212-224; Tokyo, Japan.
48. Fraidenraich G, Yacoub MD. The α-η-μ and α-κ-μ Fading Distributions. In: 2006 IEEE Ninth International Symposium on Spread Spectrum Techniques and Applications; 2006:16-20; Manaus, Brazil.
49. Moualeu JM, Costa DB, Hamouda W, Dias US, Souza RA. A performance analysis of digital communication systems over α-κ-μ fading channels. *IEEE Commun Lett*. 2019;23(1):192-195.
50. Abramowitz M, Stegun IA. *Handbook of Mathematical Functions with Formulas, Graphs, and Mathematical Tables*. Amsterdam, The Netherlands: US Government printing office; 1948.
51. Boshkovska E, Ng DWK, Zlatanov N, Schober R. Practical non-linear energy harvesting model and resource allocation for SWIPT systems. *IEEE Commun Lett*. 2015;19(12):2082-2085.
52. Li X, Li J, Liu Y, Ding Z, Nallanathan A. Residual transceiver hardware impairments on cooperative NOMA networks. *IEEE Trans Wirel Commun*. 2020;19(1):680-695.
53. Goldsmith AJ, Varaiya PP. Capacity of fading channels with channel side information. *IEEE Trans Inf Theory*. 1997;43(6): 1986-1992.
54. Valenta CR, Durgin GD. Harvesting wireless power: survey of energy-harvester conversion efficiency in far-field, wireless power transfer systems. *IEEE IEEE Microw Mag*. 2014;15(4):108-120.
55. Erceg V, Greenstein LJ, Tjandra SY, et al. An empirically based path loss model for wireless channels in suburban environments. *IEEE J Select Areas Commun*. 1999;17(7):1205-1211.
56. Stefania S, Issam T, Matthew B. *LTE–The UMTS Long Term Evolution: From Theory to Practice*. 2nd ed. New York, NY: Wiley Telecom; 2011.
57. Nauryzbayev G, Rabie KM, Abdallah M, Adebisi B. On the performance analysis of WPT-based dual-hop AF relaying networks in α-μ fading. *IEEE Access*. 2018;6:37138-37149.
58. Wolfram. The wolfram functions site; 2021. https://functions.wolfram.com/
59. Zhong C, Ratnarajah T, Wong K. Outage analysis of decode-and-forward cognitive dual-hop systems with the interference constraint in Nakagami-*m* fading channels. *IEEE Trans Veh Technol*. 2011;60(6):2875-2879.

How to cite this article: Nauryzbayev G, Omarov O, Arzykulov S, Rabie KM, Li X, Eltawil AM. Performance limits of wireless powered cooperative NOMA over generalized fading. *Trans Emerging Tel Tech*. 2022;33(4):e4415. doi: 10.1002/ett.4415

APPENDIX A. THE PDF OF A NEW RANDOM VARIABLE

Using eq. (9.6.10)[50] to represent the modified Bessel function of the first kind as

$$I_{\mu-1}\left(2\mu\sqrt{\kappa(1+\kappa)}r^{\frac{\alpha}{2}}\right)=\sum_{m=0}^{\infty}\frac{\left[\mu\sqrt{\kappa(1+\kappa)}r^{\frac{\alpha}{2}}\right]^{2m+\mu-1}}{m!\Gamma(m+\mu)}, \tag{A1}$$

and applying the "change of variable" method[57] for $X=|h_i|^2$, we can write the PDF of a new RV as

$$f_X(x)=\sum_{m=0}^{\infty}\frac{\alpha\mu^{2m+\mu}\kappa^m(1+\kappa)^{m+\mu}}{2m!\Gamma(m+\mu)e^{\mu\kappa}e^{\mu(1+\kappa)x^{\frac{\alpha}{2}}}}x^{\frac{\alpha(\mu+m)}{2}-1}. \tag{A2}$$

The same is true for the RVs Y and Z.

APPENDIX B. OUTAGE PROBABILITY FOR α-κ-μ FADING

To find the PDF of f_{W_1} in (11), we first evaluate f_{W_1} as

$$F_{W_1}=\Pr\left[\gamma_{U_2}<v\right]=\Pr\left[Z<\frac{ve_3}{e_1-ve_2}\right]=\int_0^{\frac{ve_3}{e_1-ve_2}}f_Z(z)\,\mathrm{d}z=\sum_{m=0}^{\infty}\frac{(\mu_3\kappa_3)^m\gamma\left(\mu_3+m,\Phi_3(\frac{0.5v_2e_3}{e_1-0.5v_2e_2})^{\frac{\alpha_3}{2}}\right)}{m!\Gamma(\mu_3+m)e^{\mu_3\kappa_3}}. \tag{B1}$$

Now, applying eq. (06.06.20.0003.01),[58] $f_{W_1}(v)$ can be further derived as

$$f_{W_1}(v) = \frac{dF_{W_1}}{dv} = \sum_{m=0}^{m_\infty} \frac{(\mu_3\kappa_3)^m}{m!\Gamma(\mu_3+m)e^{\mu_3\kappa_3}} \frac{\alpha_3 e_1}{2v(e_1-ve_2)} e^{-\Phi_3\left(\frac{e_3 v}{e_1-e_2 v}\right)^{\frac{\alpha_3}{2}}} \left(\Phi_3\left(\frac{e_3 v}{e_1-e_2 v}\right)^{\frac{\alpha_3}{2}}\right)^{\mu_3+m}$$
$$= \frac{I_{\mu_3-1}\left(2\mu_3\sqrt{\kappa_3(1+\kappa_3)}\left(\frac{e_3 v}{e_1-e_2 v}\right)^{\frac{\alpha_3}{4}}\right)}{v(e_1-e_2 v)\, e^{\left(\kappa_3\mu_3+\Phi_3\left(\frac{e_3 v}{e_1-e_2 v}\right)^{\frac{\alpha_3}{2}}\right)}} \left(\frac{e_3 v}{e_1-e_2 v}\right)^{\frac{\alpha_3(\mu_3+1)}{4}} \Phi_3^{\mu_3} \frac{e_1\alpha_3\mu_3\sqrt{\kappa_3(1+\kappa_3)}}{2\left(\mu_3\sqrt{\kappa_3(1+\kappa_3)}\right)^{\mu_3}}. \tag{B2}$$

The term F_{W_2} from expression (11) can be written as

$$F_{W_2} = \Pr\left[\gamma_{U_{1\to 2}} < v\right] = \Pr\left[X < \frac{V_1}{Y} + V_2\right] = \int_0^\infty f_Y(y) \int_0^{\frac{V_1}{y}+V_2} f_X(x)\mathrm{d}x\mathrm{d}y$$
$$= \sum_{n=0}^{\infty} A \sum_{m=0}^{\infty} \frac{(\mu_1\kappa_1)^m}{m!\Gamma(\mu_1+m)e^{\mu_1\kappa_1}} \int_0^\infty \frac{y^{\frac{\alpha_2(\mu_2+n)}{2}-1}}{e^{\mu_2(1+\kappa_2)y^{\frac{\alpha_2}{2}}}} \gamma\left(\mu_1+m, \Phi_1\left(\frac{V_1}{y}+V_2\right)^{\frac{\alpha_1}{2}}\right)\mathrm{d}y, \tag{B3}$$

where $V_1 = \frac{vc_4}{c_1-vc_2}$ and $V_2 = \frac{vc_3}{c_1-vc_2}$. Then, by using the series expansion of a lower incomplete Gamma function[59] as $\gamma(a,x) = \Gamma(a)\left(1-e^{-x}\sum_{L=0}^{a-1}\frac{x^L}{L!}\right)$ along with the binomial expansion theorem, F_{W_2} can be represented as

$$F_{W_2} = 1 - \left[\sum_{n=0}^{\infty}\sum_{m=0}^{\infty} \frac{A(\mu_1\kappa_1)^m}{m!e^{\mu_1\kappa_1}} \sum_{p=0}^{\mu_1+m-1} \frac{\Phi_1^p}{V_1^{-\frac{\alpha_1 p}{2}} p!} \sum_{s=0}^{\frac{\alpha_1 p}{2}} \frac{\frac{\alpha_1 p}{2}!}{\left(\frac{\alpha_1 p}{2}-s\right)!s!} \left(\frac{V_2}{V_1}\right)^{\frac{\alpha_1 p}{2}-s} \int_0^\infty y^{\frac{\alpha_2(\mu_2+n)}{2}-s-1} e^{-\Phi_2 y^{\frac{\alpha_2}{2}}} e^{-\Phi_1\left(\frac{V_1}{y}+V_2\right)^{\frac{\alpha_1}{2}}}\mathrm{d}y\right]. \tag{B4}$$

Furthermore, applying the binomial approximation

$$\left(1+\frac{V_1}{V_2}y^{-1}\right)^{\frac{\alpha_1}{2}} \approx 1+\frac{\alpha_1}{2}\frac{V_1}{V_2}y^{-1}, \tag{B5}$$

eq. (3.6.9)[50] and the following equalities, as in eq. (01.03.26.0004.01),[58]

$$e^{-\Phi_2 y^{\frac{\alpha_2}{2}}} = G_{0,\,1}^{1,\,0}\left(\Phi_2 y^{\frac{\alpha_2}{2}} \middle| \begin{matrix} - \\ 0 \end{matrix}\right), \tag{B6}$$

$$e^{-\Phi_1 V_2^{\frac{\alpha_1}{2}-1} V_1^{\frac{\alpha_1}{2}} y^{-1}} = G_{1,\,0}^{0,\,1}\left(\frac{2y}{\Phi_1 V_2^{\frac{\alpha_1}{2}-1}\alpha_1 V_1} \middle| \begin{matrix} 1 \\ - \end{matrix}\right), \tag{B7}$$

F_{W_2} can be solved using eq. (21).[47] Then, inserting (B2) and (B4) into (11), the exact outage can be rewritten as in (12).

APPENDIX C. HIGH-SNR APPROXIMATION OF OUTAGE PROBABILITY

The expression of D_2 in (15) is re-calculated as

$$D_2 = \sum_{n=0}^{\infty} A \sum_{m=0}^{\infty} \frac{(\mu_1\kappa_1)^m}{m!\Gamma(\mu_1+m)e^{\mu_1\kappa_1}} \int_0^\infty \frac{y^{\frac{\alpha_2(\mu_2+n)}{2}-1}}{e^{\mu_2(1+\kappa_2)y^{\frac{\alpha_2}{2}}}} \gamma\left(\mu_1+m, \Phi_1\left(\frac{\phi_1}{y}+\phi_2\right)^{\frac{\alpha_1}{2}}\right)\mathrm{d}y. \tag{C1}$$

Assuming the high-SNR regime, the expression given by $\Phi_1\left(\phi_1\left(y^{-1}+\frac{\phi_2}{\phi_1}\right)\right)^{\frac{\alpha_1}{2}}$ tends to zero, where $\frac{\phi_2}{\phi_1}$ is a constant and $\phi_1 \to 0$. Taking into account that $\gamma(c,d) \approx \frac{d^c}{c}$, when $d \to 0$,[59] the expression in (C1) can be simplified using the binomial expansion theorem and the definition of a Gamma function mentioned earlier as

$$D_2 = \sum_{n=0}^{\infty} A \sum_{m=0}^{\infty} \frac{(\mu_1\kappa_1)^m \left(\Phi_1 \phi_1^{\frac{\alpha_1}{2}}\right)^{\mu_1+m}}{m!\Gamma(\mu_1+m)e^{\mu_1\kappa_1}(\mu_1+m)} \sum_{r=0}^{\frac{\alpha_1(\mu_1+m)}{2}} \frac{\frac{\alpha_1(\mu_1+m)}{2}!}{(\frac{\alpha_1(\mu_1+m)}{2}-r)!r!} \left(\frac{\phi_2}{\phi_1}\right)^{\frac{\alpha_1(\mu_1+m)}{2}-r} \frac{2}{\alpha_2(\Phi_2)^{\mu_2+n-\frac{2r}{\alpha_2}}} \Gamma\left(\mu_2+n-\frac{2r}{\alpha_2}\right). \quad \text{(C2)}$$

In a similar manner to (B1), the expression of D_1 in (14) can be further rewritten as

$$D_1 = \sum_{m=0}^{\infty} \frac{(\mu_3\kappa_3)^m}{m!\Gamma(\mu_3+m)e^{\mu_3\kappa_3}} \gamma\left(\mu_3+m, \Phi_3\left(\frac{0.5v_2e_3}{e_1-0.5v_2e_2}\right)^{\frac{\alpha_3}{2}}\right). \quad \text{(C3)}$$

Now, applying the high-SNR approximation mentioned above to (C3) leads to

$$D_1 = \sum_{m=0}^{\infty} \frac{(\mu_3\kappa_3)^m \left(\Phi_3(\frac{0.5v_2e_3}{e_1-0.5v_2e_2})^{\frac{\alpha_3}{2}}\right)^{\mu_3+m}}{m!\Gamma(\mu_3+m)e^{\mu_3\kappa_3}(\mu_3+m)}. \quad \text{(C4)}$$

The high-SNR asymptotic OP expression $P_{\text{out},2}^{HS}$ can be expressed as in (C5), where $M = \frac{2\left(\frac{\alpha_1(\mu_1+m)}{2}\right)!}{\alpha_2\left(\frac{\alpha_1(\mu_1+m)}{2}-r\right)!r!}$.

$$P_{\text{out},2}^{HS} = 1 - \left[1 - \sum_{n=0}^{n_\infty}\sum_{m=0}^{m_\infty} \frac{A(\mu_1\kappa_1)^m \left(\Phi_1\phi_1^{\frac{\alpha_1}{2}}\right)^{\mu_1+m}}{m!\Gamma(\mu_1+m)e^{\mu_1\kappa_1}(\mu_1+m)} \sum_{r=0}^{\frac{\alpha_1(\mu_1+m)}{2}} \left(\frac{\phi_2}{\phi_1}\right)^{\frac{\alpha_1(\mu_1+m)}{2}-r} M \frac{\Gamma\left(\mu_2+n-\frac{2r}{\alpha_2}\right)}{\Phi_2^{\mu_2+n-\frac{2r}{\alpha_2}}}\right] \times \left[1 - \sum_{m=0}^{m_\infty} \frac{(\mu_3\kappa_3)^m \left(\Phi_3\left(\frac{0.5v_2e_3}{e_1-0.5v_2e_2}\right)^{\frac{\alpha_3}{2}}\right)^{\mu_3+m}}{m!\Gamma(\mu_3+m)e^{\mu_3\kappa_3}(\mu_3+m)}\right] \quad \text{(C5)}$$

APPENDIX D. ERGODIC CAPACITY ANALYSIS

D.0.1 *S*-to-U_2 link

For the direct *S*-to-U_2 link, the ergodic capacity expression is defined as

$$\begin{aligned} C_{\text{erg}}^{\gamma_{U_2}} &= \int_0^{\infty} H_p \log_2\left(1+\gamma_{U_2}\right) f_{\gamma_{U_2}} \mathrm{d}\gamma_{U_2} \\ &= \int_0^{\infty} H_p \log_2(e_3+(e_1+e_2)Z) f_G(\mathrm{g})\mathrm{dg} - \int_0^{\infty} H_p \log_2(e_3+e_2Z) f_Q(q)\mathrm{d}q \\ &= \frac{H_p}{\ln(2)}\left[\int_0^{\infty} \ln\left(1+\frac{\mathrm{g}}{e_3}\right) f_G(\mathrm{g})\mathrm{dg} - \int_0^{\infty} \ln\left(1+\frac{q}{e_3}\right) f_Q(q)\mathrm{d}q\right], \end{aligned} \quad \text{(D1)}$$

where $G = EZ$ and $Q = e_2Z$ and their PDFs are defined as $f_G(\mathrm{g}) = \frac{1}{E} f_Z(\frac{\mathrm{g}}{E})$ and $f_Q(q) = \frac{1}{e_2} f_Z(\frac{q}{e_2})$, respectively.

Noticing the similarity in a structure of $f_G(g)$ and $f_Q(q)$, we write

$$f_G(g) = \sum_{c=0}^{\infty} DE^{-\frac{\alpha_3(\mu_3+c)}{2}} g^{\frac{\alpha_3(\mu_3+c)}{2}-1} e^{-\Phi_3\left(\frac{g}{E}\right)^{\frac{\alpha_3}{2}}}. \tag{D2}$$

Using eq. (11),[47] given by

$$\ln(1+a) = G_{2,\,2}^{1,\,2}\left(a \middle| \begin{matrix} 1,\ 1 \\ 1,\ 0 \end{matrix}\right), \tag{D3}$$

and eq. (21),[47] the first integral in (D1) can be expressed as in (D4), where α_3 is an even number. Extrapolating the obtained results to the case of a variable q and further substituting them gives the general ergodic capacity expression for a generalized α-κ-μ fading model as shown in (18).

$$\int_0^{\infty} \ln\left(1+\frac{g}{e_3}\right) f_G(g)\,\mathrm{d}g = \sum_{c=0}^{\infty} D \frac{\left(\frac{e_3}{E}\right)^{\frac{\alpha_3(\mu_3+c)}{2}} \frac{2}{\alpha_3}}{(2\pi)^{\frac{\alpha_3}{2}-1}} G_{\alpha_3,\ \alpha_3+1}^{\alpha_3+1,\ \frac{\alpha_3}{2}}\left(\Phi_3\left(\frac{e_3}{E}\right)^{\frac{\alpha_3}{2}} \middle| \begin{matrix} \Delta(\frac{\alpha_3}{2},-\zeta_3),\ \Delta(\frac{\alpha_3}{2},1-\zeta_3) \\ 0,\ \Delta(\frac{\alpha_3}{2},-\zeta_3),\ \Delta(\frac{\alpha_3}{2},-\zeta_3) \end{matrix}\right) \tag{D4}$$

$$\begin{aligned} C_{\mathrm{erg,}Asym}^{\gamma_{U_{1\to 2}}} = \frac{H_p}{\ln(2)} \Bigg[& \sum_{m=0}^{m_\infty} B \frac{\left(\frac{c_3}{c_5}\right)^{\frac{\alpha_1(\mu_1+m)}{2}} \frac{2}{\alpha_1}}{(2\pi)^{\frac{\alpha_1}{2}-1}} G_{\alpha_1,\ \alpha_1+1}^{\alpha_1+1,\ \frac{\alpha_1}{2}}\left(\Phi_1\left(\frac{c_3}{c_5}\right)^{\frac{\alpha_1}{2}} \middle| \begin{matrix} \Delta(\frac{\alpha_1}{2},-\zeta_1),\ \Delta(\frac{\alpha_1}{2},1-\zeta_1) \\ 0,\ \Delta(\frac{\alpha_1}{2},-\zeta_1),\ \Delta(\frac{\alpha_1}{2},-\zeta_1) \end{matrix}\right) \\ & - \sum_{m=0}^{m_\infty} B \frac{\left(\frac{c_3}{c_2}\right)^{\frac{\alpha_1(\mu_1+m)}{2}} \frac{2}{\alpha_1}}{(2\pi)^{\frac{\alpha_1}{2}-1}} G_{\alpha_1,\ \alpha_1+1}^{\alpha_1+1,\ \frac{\alpha_1}{2}}\left(\Phi_1\left(\frac{c_3}{c_2}\right)^{\frac{\alpha_1}{2}} \middle| \begin{matrix} \Delta(\frac{\alpha_1}{2},-\zeta_1),\ \Delta(\frac{\alpha_1}{2},1-\zeta_1) \\ 0,\ \Delta(\frac{\alpha_1}{2},-\zeta_1),\ \Delta(\frac{\alpha_1}{2},-\zeta_1) \end{matrix}\right) \Bigg] \end{aligned} \tag{D5}$$

D.0.2 U_1-to-U_2 link

The general ergodic capacity expression for U_1-to-U_2 link is

$$\begin{aligned} C_{\mathrm{erg}}^{\gamma_{U_{1\to 2}}} &= \int_0^{\infty} H_p \log_2\left(1+\gamma_{U_{1\to 2}}\right) f_{\gamma_{U_{1\to 2}}} \mathrm{d}\gamma_{U_{1\to 2}} \\ &= \int_0^{\infty} H_p \log_2\left(c_4 + (c_1+c_2)XY\right) f_T(t)\mathrm{d}t - \int_0^{\infty} H_p \log_2\left(c_4 + c_2 XY\right) f_V(v)\mathrm{d}v \\ &= \frac{H_p}{\ln(2)}\left[\int_0^{\infty} \ln\left(1+\frac{t}{c_4}\right) f_T(t)\mathrm{d}t - \int_0^{\infty} \ln(1+\frac{v}{c_4}) f_V(v)\mathrm{d}v\right], \end{aligned} \tag{D6}$$

where $T = c_5XY$ and $V = c_2XY$ are new RVs.

The PDF of T is defined as

$$f_T(t) = \int_0^{\infty} \frac{1}{yc_5} f_Y(y) f_X\left(\frac{t}{yc_5}\right) \mathrm{d}y. \tag{D7}$$

Due to their similarity, the thorough derivation of the PDF is shown only for the variable t. Making $\alpha_1 = \alpha_2 = \alpha$, and using eq. (3.478.4),[46] the new PDF for α-κ-μ fading is written as

$$f_T(t) = \sum_{m=0}^{\infty} B \sum_{n=0}^{\infty} A\Lambda \left(\frac{1}{c_1+c_2}\right)^{\beta} t^{\frac{\alpha(\mu_2+n+\mu_1+m)}{4}-1} K_{\mu_2+n-\mu_1-m}\left(2\sqrt{\Phi_1\Phi_2\left(\frac{1}{c_1+c_2}\right)^{\frac{\alpha}{2}} t^{\frac{\alpha}{4}}}\right), \tag{D8}$$

where $K_\nu(\cdot)$ denotes the modified Bessel function of the second kind and order ν.

In the same manner, as part of the capacity derivation process, using (D3) and $K_\nu(a) = \frac{1}{2} G_{0,\,2}^{2,\,0}\left(\frac{a^2}{4}\middle|\begin{matrix}-,\\ \frac{\nu}{2},\end{matrix}\ \begin{matrix}-\\ -\frac{\nu}{2}\end{matrix}\right)$ from eq. (14)[47] as a replacement, we can further express the first integral in (D6) as in (D9). Moreover, applying eq. (21),[47] the integral in (D9) is solved. Extrapolating the obtained results to the case of variable ν and further substituting them gives us the general ergodic capacity expression for a generalized α-κ-μ fading model, as shown in (21).

$$\int_0^\infty \ln\left(1+\frac{t}{c_4}\right) f_T(t)\mathrm{d}t = \sum_{m=0}^{\infty} B \sum_{n=0}^{\infty} A\Lambda \frac{\left(\frac{c_4}{c_5}\right)^\beta}{\alpha(2\pi)^{\frac{\alpha}{2}-1}} G_{\alpha,\ \alpha+2}^{\alpha+2,\ \frac{\alpha}{2}}\left(\Phi_1\Phi_2\left(\frac{c_4}{c_5}\right)^{\frac{\alpha}{2}}\middle|\begin{matrix}\Delta(\frac{\alpha}{2},-\xi),\ \Delta(\frac{\alpha}{2},1-\xi)\\ \frac{\mu_2-\mu_1}{2},\ \frac{\mu_1-\mu_2}{2},\ \Delta(\frac{\alpha}{2},-\xi),\ \Delta(\frac{\alpha}{2},-\xi)\end{matrix}\right)$$

Additionally, the asymptotic capacity of the U_1-to-U_2 link is evaluated to be explicit. As a result, the SINDR at U_2 is changed to

$$\gamma_{U_{1\to 2}} = \frac{c_1 X}{c_2 X + c_3}, \tag{D10}$$

accounting for $c_4 \to 0$. Due to the similarity of the general form of the asymptotic SINDR with the previously mentioned direct transmission case, the explanations are omitted here. The asymptotic expression of the average capacity related to the U_1-to-U_2 link is shown in (D5), where $\zeta_1 = \frac{\alpha_1(\mu_1+m)}{2}$.